

**Rainfall Estimation Over Oceans
From Scanning Multichannel Microwave
Radiometer and Special Sensor
Microwave/Imager Microwave Data**

**C. Prabhakara, G. Dalu, G. L. Liberti,
J. J. Nucciarone, and R. Suhasini**

August 1991

(NASA-TM-104546) RAINFALL ESTIMATION OVER
OCEANS FROM SCANNING MULTICHANNEL MICROWAVE
RADIOMETER AND SPECIAL SENSOR
MICROWAVE/IMAGER MICROWAVE DATA (NASA)

69 p

CSC 04B G3/47

N91-30646

Unclass
0036884

NASA

NASA Technical Memorandum 104546

**Rainfall Estimation Over Oceans
From Scanning Multichannel Microwave
Radiometer and Special Sensor
Microwave/Imager Microwave Data**

**C. Prabhakara, G. Dalu, G. L. Liberti,
J. J. Nucciarone, and R. Suhasini**

August 1991



ABSTRACT

Based on the above considerations, 37-GHz observations with a 30 km fov from SMMR and SSM/I are selected for the purpose of rain rate retrieval over oceans. An empirical method is developed to estimate the rain rate, in which it is assumed that over an oceanic area, the statistics of the observed T_b 's at 37 GHz in a rain storm are related to the rain rate statistics in that storm. Also, in this method, the underestimation of rain rate, arising from the inability of the radiometer to respond sensitively to rain rate above a given threshold, is rectified with the aid of two parameters that depend on the total water vapor content in the atmosphere. The rain rates retrieved by this method compare favorably with radar observations. Monthly mean global maps of rain derived from this technique over the oceans are consistent with climatology.

Table of Contents

1. Introduction	1
2. Theoretical Background and Inferences	
From Satellite Observations	6
a. Observations	9
b. Radiative Transfer Simulations	14
c. Inferences	21
3. Spatial Distribution of Rain and Its Impact	
on Microwave Observations	23
4. Rain Retrieval Algorithm for the Oceans	34
5. Application to Case Studies	40
6. Discussion and Conclusion	50
Appendix	55
References	61

1. Introduction

Information about rainfall over the oceans is needed in several types of investigations. In addition to being an important element of the global hydrological cycle, rainfall over the oceans is of considerable interest in studies relating to ocean-atmosphere interactions, interannual variations of climate, El Niño events, and other climate changes (see, for example, Lau and Chan, 1988). Despite its importance, complete information about rainfall over the oceans is not readily available. Climatologies have been deduced indirectly from ship observations, but these observations are inherently nonuniformly distributed (Tucker, 1961; Dorman and Bourke, 1979, 1981; Reed and Elliott, 1979; Mintz, 1981). A satellite based climatology from Nimbus-5 ESMR microwave measurements was attempted by Rao et al. (1976), but these estimates were never properly validated (Wilheit et al., 1991).

There are a few carefully planned rainfall measuring experiments with radars and rain gauges over the oceans, such as GATE (Hudlow and Patterson, 1979). These are inadequate to develop the climatology of rain over oceans. Satellite remote sensing of rain similar to that planned for the Tropical Rainfall Measurement Mission (TRMM) (Simpson, 1988) should improve this situation considerably. However, the remote sensing method needed for TRMM involving passive microwave radiometry is not fully developed.

Visible and infrared (VIS/IR) satellite observations have been analyzed to estimate rainfall by several investigators (see, for example, Kilonsky and Ramage, 1975; Arkin, 1979; Adler and Negri, 1988). However, in these spectral regions, the clouds tend to be opaque and, hence, rainfall must be inferred indirectly. For example, in a method called the Area Time Integral (ATI) (Doneaud et al., 1984; Lopez et al., 1989; Atlas et al., 1990a), the total volume of rain in a given region is estimated from the time-averaged rain cloud area and the duration of the rain event. For satellite applications, the rain cloud area is taken to be the area that has a temperature below a specified threshold. This threshold is selected on a statistical basis that optimizes the cloud area-rainfall relationship. For example the Global Precipitation Index (GPI) method of Arkin (1979) is a simplified application of the ATI approach. Currently this method is being used to provide global operational rainfall data sets (Arkin and Meisner, 1987).

Because the VIS/IR techniques are indirect, it is useful to understand how such estimates of rain compare to those derived from microwave radiometers. Therefore, the goal of this study is to develop a satellite-based method to sense rain from the existing data taken by the Scanning Multichannel Microwave Radiometer (SMMR) flown on Nimbus 7 (Gloersen and Hardis, 1978) and the Special Sensor Microwave/Imager (SSM/I) flown on the Defense Meteorological Satellite Program (DMSP) Block 5D-2 satellite (Hollinger et al., 1987).

The microwave region, particularly at frequencies at or below 37 GHz, is not as opaque to the clouds and rain as the visible and infrared spectral regions. The hydrometeors in the clouds and rain layers have microwave absorption, emission, and scattering properties, which can be used to derive information about rain. For this reason, the information about rain, based on passive microwave measurements in the frequency range between 6.6 and 85 GHz is examined here on a large scale with data composited from SMMR and SSM/I. This analysis is necessary to select the microwave frequencies best suited for rain retrieval over oceans.

The brightness temperature (T_b) measurements at 37 GHz, having a field of view (fov) of about 30 km, show relatively strong emission from rain, reaching values as large as 260 K over the tropical and midlatitude rainbelts. Only marginal effects caused by scattering by ice above the rain clouds are revealed. At frequencies below 37 GHz, where the fov is much larger than 30 km and the extinction is weaker, T_b is significantly smaller than 260 K. At these low frequencies, scattering by ice is not noticeable. Additional information about rain gained from these low frequency channels is not appreciable. On the other hand, at 85 GHz (fov \cong 15 km), where the extinction is very strong, the sea surface below the clouds is often masked and scattering from ice above the rain clouds is vividly noticed. However, these high-frequency measurements do not yield direct information about rain below the clouds.

Another important consideration in sensing rain is that the satellite-borne passive microwave radiometers have a field of view that is much larger than the scale of the rain cells, which are typically a few kilometers in size. Rain rates associated with different rain cells, present in the fov of the radiometer at a given time, can vary widely. Additionally, when the rain rate exceeds some value, radiometer response reaches saturation and the brightness temperature does not increase sensitively with further increase in the rain rate. At 37 GHz, loss of sensitivity happens when T_b is around 260 K. The combined effects of the areal distribution of rain rate in the fov and the sensitivity of the radiometer to rain rate, are inherently contained in the observations made by the radiometer. For these reasons, the average rain rate in the fov of a satellite-borne microwave radiometer is systematically underestimated.

To overcome these problems, an empirical method is developed to sense rain rate from SMMR and SSM/I data, which incorporates a rectification for the systematic underestimation. Rain rate statistics from GATE are used to tune this method. As a check, rain rates estimated with this method are compared with those deduced from radar. Seasonal mean global rainfall maps over oceans obtained with this approach, from 50°N to 50°S, are consistent with the climatological maps.

We are thankful to Prof. Eric Smith, whose thorough examination and valuable comments added much to this work, and to

Dr. Christian Kummerow for allowing us to use his radiative transfer model in our research.

2. Theoretical Background and Inferences From Satellite Observations

Models of the microwave radiative transfer in the atmosphere containing clouds and rain above the sea surface have been developed in several studies (Savage, 1976; Wilheit et al., 1977; Tsang et al., 1977; Wu and Weinman, 1984; Olson, 1987; Smith and Mugnai, 1988; Kummerow et al., 1989). Given the vertical stratification of the hydrometeors and the atmospheric conditions, it is possible to compute the upwelling brightness temperatures emerging from the top of the atmosphere with the help of radiative transfer theory, assuming horizontal homogeneity. However, rain is highly variable in space and time and, as a consequence, rain systems most often exhibit a large variation in the spatial distribution of cloud liquid water and in the amount of ice and supercooled liquid water above the rain layers. Since the spatial distribution of all the hydrometeors is not available in detail, in the theoretical simulation of brightness temperature, a simple variation of the hydrometeors in the horizontal is generally assumed as a practical approach.

In order to appreciate the information conveyed by the SMMR and SSM/I data, it is essential to know the absorption and scattering properties of the hydrometeors over the frequency range of interest. These properties are presented in Fig. 1. It is evident that at all frequencies, raindrop absorption is much larger than that of ice

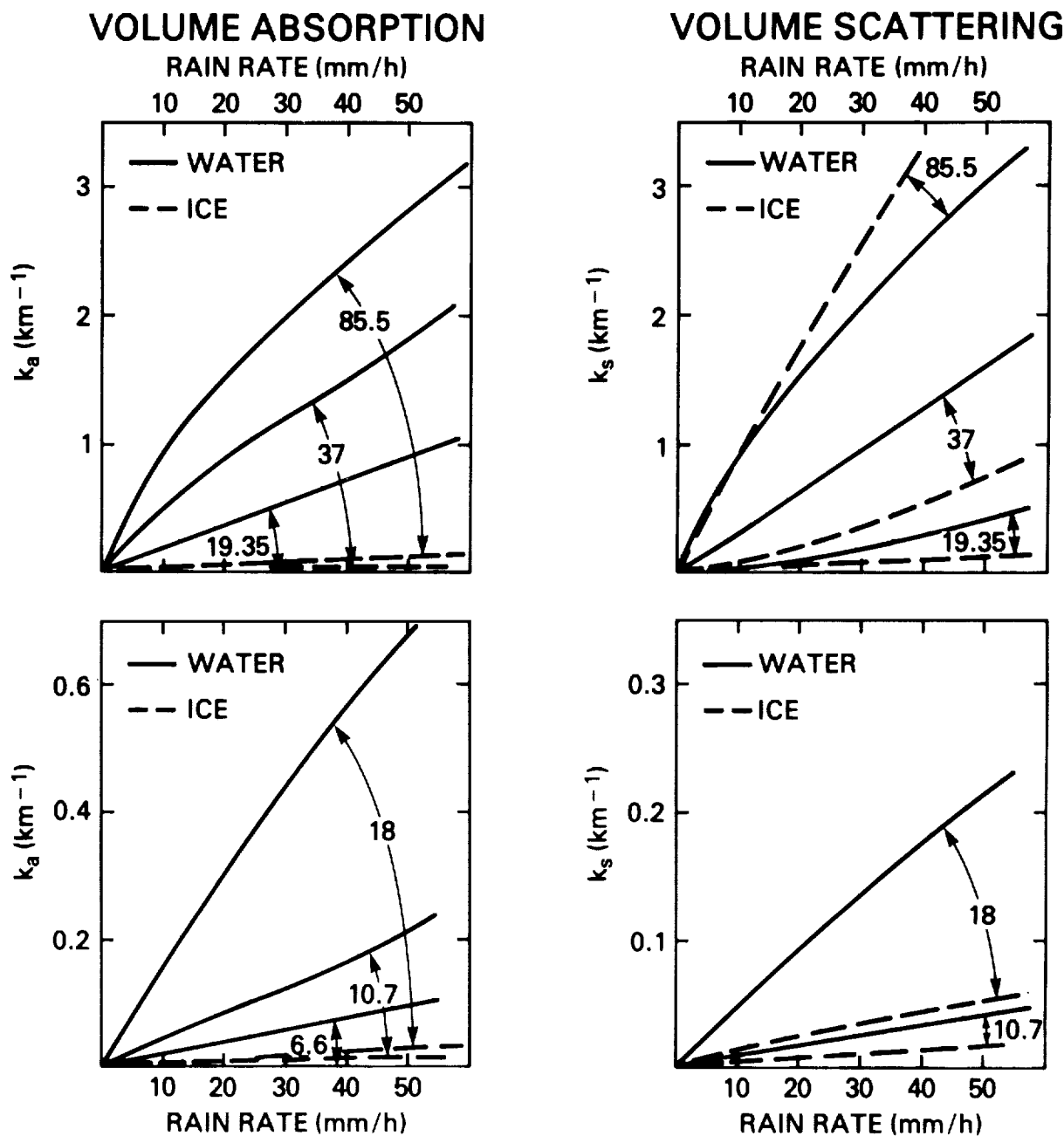


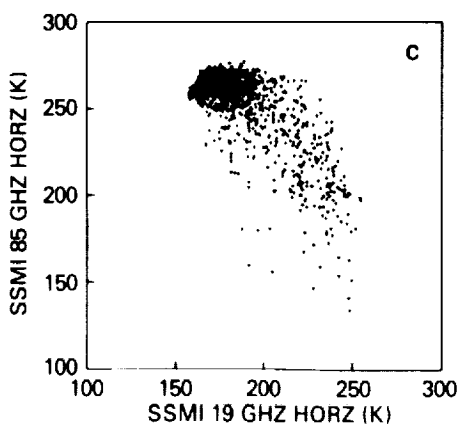
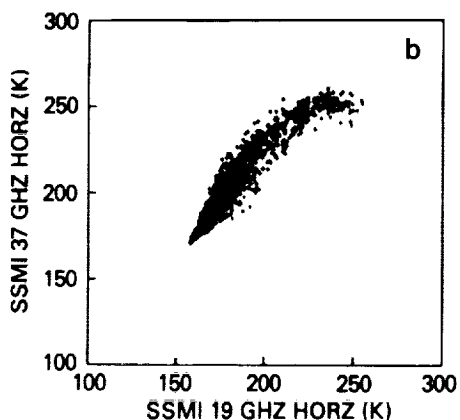
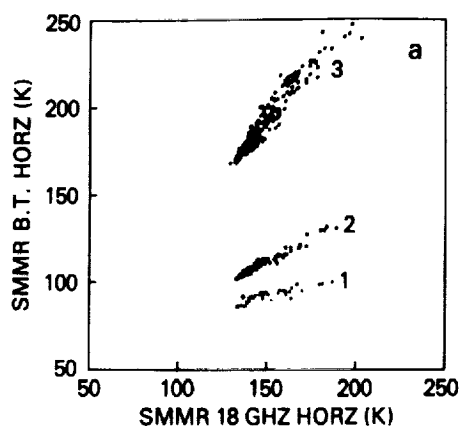
Figure 1. - Volume absorption and scattering coefficients, k_a (km^{-1}) and k_s (km^{-1}), in the microwave region between 6.6 and 85 GHz (based on: Olson, 1987; Spencer et al., 1989).

particles. Thus, the thermal emission of the hydrometeors at all frequencies will be mainly from water particles. Ice particles, on the other hand, can make a significant contribution to the scattering of microwave radiation. At 85.5 GHz, ice scattering exceeds that of water drops. Typically, at rain rates below about 20 mm/h, the ice scattering coefficient at 85 GHz is an order of magnitude larger than that at 37 GHz. Both the absorption and scattering coefficients for water and ice particles increase as a function of the rain rate and frequency. These absorption and scattering properties are important factors that govern the radiative transfer in the microwave region.

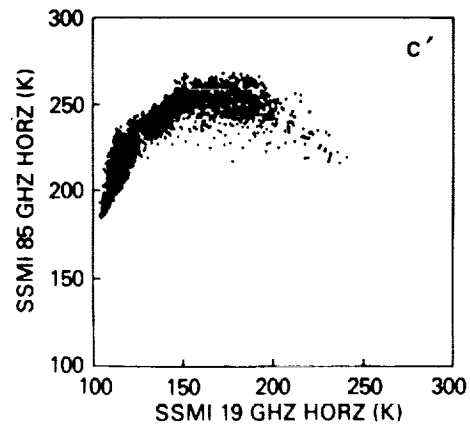
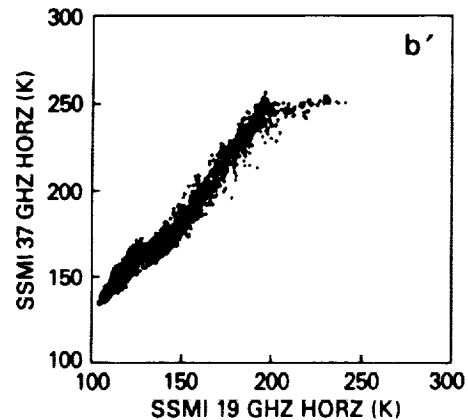
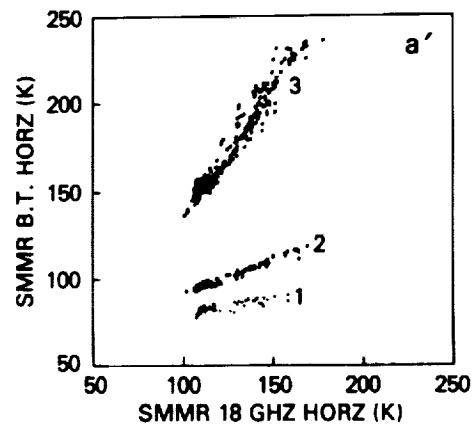
SMMR and SSM/I data also contain useful information in the polarization measurements at different frequencies. The sea surface emissivity, which is significantly less than unity in the microwave region, has an angular dependence. Moreover, the horizontal and vertical polarization components emitted by the sea surface away from nadir differ appreciably from one another (e.g., Wilheit, 1979). Since both the SMMR and SSM/I antennas subtend an incidence angle of about 50° at the sea surface, their polarization components differ markedly. This information can be revealed by these satellite radiometers when the surface is not obscured by the atmospheric extinction caused by hydrometeors. As the atmospheric opacity increases, at any frequency, the difference between the horizontal and vertical polarization measurements made at the top of the atmosphere decreases, and eventually vanishes. This occurs when the hydrometeors do not influence the radiation with their own polarization.

a. Observations

Given the above background, let us assess the independent information about the hydrometeors that is contained in the passive microwave multifrequency dual-polarization observations made by SMMR and SSM/I. For this purpose, the data obtained by SMMR and SSM/I during the period of July and August 1987, when both of the instruments were functioning simultaneously, are examined closely in Figs. 2 and 3. The data shown in these figures are taken from two oceanic areas, each measuring 3° lat x 5° long. This area size and length of time yielded a satisfactory sample size in all channels, as shown in the figures. The two oceanic areas chosen, one in the Inter-Tropical Convergence Zone (ITCZ) and the other in the midlatitude rain belt of the North Pacific, indicated substantial precipitation activity. The 6.6-, 10.7-, and 37-GHz brightness temperatures (T_6 , T_{10} , and T_{37}) of SMMR are plotted against 18-GHz brightness temperatures (T_{18}) and are shown separately for the two areas in Fig. 2, a and a'. The SSM/I T_{37} and T_{85} are analyzed similarly by plotting them against T_{19} in Fig. 2, b, c, and b', c'. All of the data shown in Fig. 2 are polarized in the horizontal direction. The satellite data shown in the figure indicate the response of the various channels to meteorological conditions that ranged from almost clear skies to heavy rain. However, one should remember that the fov is different for each channel and is such that it increases in size as the frequency of the channel decreases, and the absorption from rain drops increases as the frequency increases (Fig. 1).



ITCZ in Eastern Pacific



North Central Pacific

Figure 2. - Comparison of brightness temperature observations in the horizontal polarization:

- a & a' 1. SMMR 18.0 GHz at 68 km fov vs. 6.6 GHz at 155 km fov;
- 2. SMMR 18.0 GHz at 68 km fov vs. 10.7 GHz at 95 km fov;
- 3. SMMR 18.0 GHz at 68 km fov vs. 37.0 GHz at 60 km fov;
- b & b' SSM/I 19.3 GHz vs. 37.0 GHz, fov 60 km vs. 30 km;
- c & c' SSM/I 19.3 GHz vs. 85.5 GHz, fov 60 km vs. 15 km.
- a, b, c are for 6° - 9° N, 90° - 95° W;
- a', b', c' are for 42° - 45° N, 160° - 165° W.

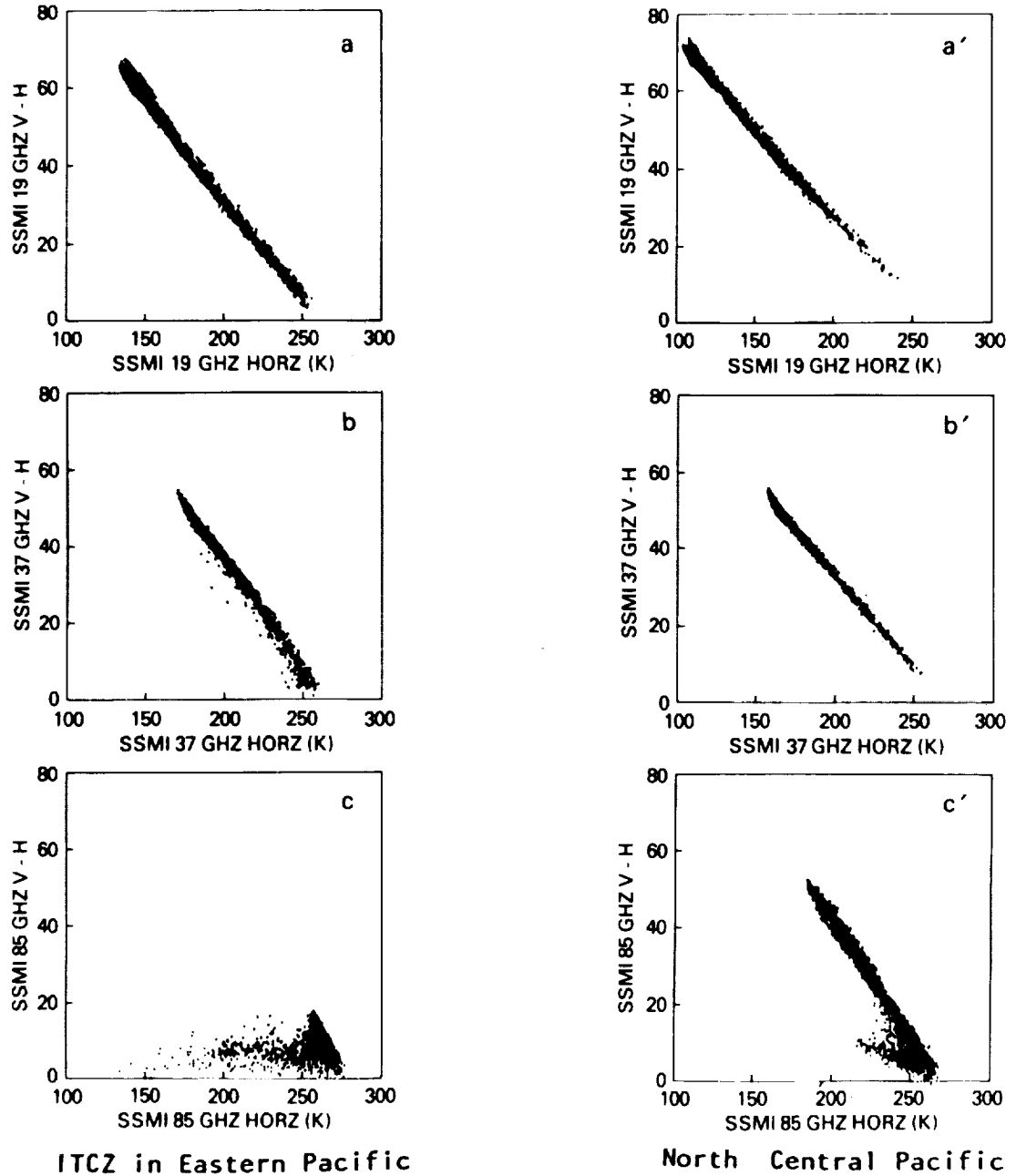


Figure 3. - Observations of polarization difference in brightness temperature ($T_V - T_H$) (K) vs. T_H (K) for 19.3, 37 and 85.5 GHz SSM/I channels:

- a & a' ($T_V - T_H$) vs. T_H at 19.3 GHz;
- b & b' ($T_V - T_H$) vs. T_H at 37.0 GHz;
- c & c' ($T_V - T_H$) vs. T_H at 85.5 GHz.
- a, b, c are for $6^\circ - 9^\circ$ N and $90^\circ - 95^\circ$ W;
- a', b', c' are for $42^\circ - 45^\circ$ N and $160^\circ - 165^\circ$ W.

From Fig. 2, a and a', we notice that in the low-frequency channels (6.6, 10.7, and 18 GHz), where the fov \geq 60 km, brightness temperature T_b measured in different channels shows a linear dependence on one another. We find T_b 's at higher frequencies to be generally larger than those at lower frequencies; however, T_b rarely exceeds a value of 260 K. We notice also that the 37-GHz channel, when compared to the 18-GHz channel at 60-km fov, shows approximately the same linear dependence on T_{18} until T_{37} is equal to about 260 K, where it appears to reach a maximum. This maximum in T_b is descriptively called saturation. The plot of SSM/I observations at 19 and 37 GHz, as shown in Fig. 2, b and b', reveals distinctly the saturation in the 37-GHz channel around 260 K (unlike the SMMR data shown in Fig. 2, a, the 37-GHz data of SSM/I have a 30-km fov, while the corresponding 19-GHz data have an fov of 60 km). The near linear dependence of 37-GHz data on 19-GHz, until saturation is reached in T_{37} , reinforces the relationship between the 18- and 37-GHz channels seen in the SMMR data. Deviations from this dominant linear trend may be caused, in part, by differences in the fov.

The approximate linear relationship between T_{37} and T_{19} is examined statistically at several locations over the global oceans. The correlation coefficient between T_{19} and T_{37} is generally high, larger than about 0.9. The SSM/I samples used in this correlation study cover the region 50°N to 50°S. Each sample represents data for one month over an oceanic region of 3° lat x 5° long. From the above

discussion, we find that the T_b 's at frequencies $\nu \leq 37$ GHz exhibit a near linear relationship, and, hence, they are highly redundant.

The data taken from SSM/I at 85 and 19 GHz are compared in Fig. 2, c and c'. (Note that the fov of the 85-GHz data is 15 km while that of the 19-GHz data is 60 km). The 85-GHz data in the tropics (Fig. 2, c) show a large variability with respect to the 19-GHz measurements. The saturation in 85-GHz brightness temperature is close to a value of 270 K, and this occurs when T_{19} is about 190 K. Also, one notices a negative slope between the 85-GHz and 19-GHz data beyond the saturation point of the 85-GHz data. This negative slope is also evident when 85-GHz data are compared with the data at 37 GHz, which have a 30-km fov. Fig. 2, c', which corresponds to the analysis of 85- and 19-GHz data from SSM/I in the midlatitude rain area, also shows saturation in the 85-GHz data and a weak negative slope beyond that point.

The polarization difference $\delta = (T_V - T_H)$ between the vertical and horizontal components at 19, 37, and 85 GHz, taken from SSM/I data, are presented in Fig. 3, a-c and a'-c'. In this figure, the panels a, b, and c correspond to the ITCZ, while the panels a', b', and c' correspond to the midlatitude rain region. The polarization difference δ at 19 and 37 GHz, in both the ITCZ and midlatitude rain areas, shows a linear dependence on the brightness temperature T_H with a negative slope. In the tropics, some minor deviations from the linear trend are noticed at 37 GHz (see Fig. 3, b). In general, δ tends to have small values as T_H increases to about 260 K in the

19- and 37-GHz channels. In contrast to this, the bulk of the data at 85 GHz indicates a decrease in δ as T_{85} increases to about 270 K; around that point, the polarization difference is near zero. The remaining 85-GHz data in the tropics are spread between $T_{85} \cong 270$ K and some small values at about 150 K, and indicate no correlation with the polarization difference δ . This feature is more pronounced in the tropics than in the midlatitudes.

b. Radiative Transfer Simulations

In an attempt to probe the meaning of the SMMR and SSM/I multifrequency dual-polarization brightness temperatures, radiative transfer calculations have been performed using the theoretical model of Kummerow et al. (1989). These theoretical results are presented in Figs. 4 and 5. The salient parameters that enter into these computations are rain rate, fraction of the fov covered by rain, sea-surface wind speed, cloud-liquid water content, water vapor in the atmosphere, and sea-surface temperature (SST). Each parameter is changed over a range as specified in Table 1. One hundred radiative transfer simulations are made for each class shown in the table by randomly changing the values of each parameter within the range specified. The atmospheric temperature and humidity profiles adopted for these computations correspond to a tropical profile with a lapse rate of 6.5° C per km. The incidence angle at the sea surface is 49° . The SST is 298 K and the freezing level is assumed to be at 4-km altitude. In this theoretical model, it is assumed that, when there is rain, there is a mixed phase of hydrometeors above the

freezing level up to an altitude where the temperature reaches 238 K. Above that altitude, only ice phase hydrometeors are present.

Table 1. - Range in Magnitude of the Variables for Each Class

Class	Rain Rate mm/h	Fraction of fov	Wind (m/s)	CLW (g/cm ³)	RH %	SST K
O	0	0	0 - 10	0 - 0.6	100	292-303
A	0 - 3	0.6 - 1	0 - 15	0 - 0.6	100	298
B	3 - 6	0.8 - 1	0 - 15	0 - 0.6	100	298
C	6 - 12	1	0 - 15	0 - 0.6	100	298
D	12 - 24	1	0 - 15	0 - 0.6	100	298

Variables are rain rate, fractional fov with rain, sea-surface wind speed, cloud-liquid water content (CLW), relative humidity (RH), and sea-surface temperature (SST).

The amount of different hydrometeors in the mixed phase and ice phase depends on rain rate and is assumed to systematically decrease as a function of altitude (see Kummerow et al., 1989). In order to cover a significant dynamic range in rain rates, these computations are performed for five successive classes for rain rates starting from 0 mm/h to a maximum of 12-24 mm/h. In these computations, the fov at all microwave frequencies is assumed to be the same. The rain rate in the fraction of the fov that has rain is assumed to have one value. The results obtained from 100 computations for each class are presented in Figs. 4 and 5. One may note that the random variation of some of the parameters in these

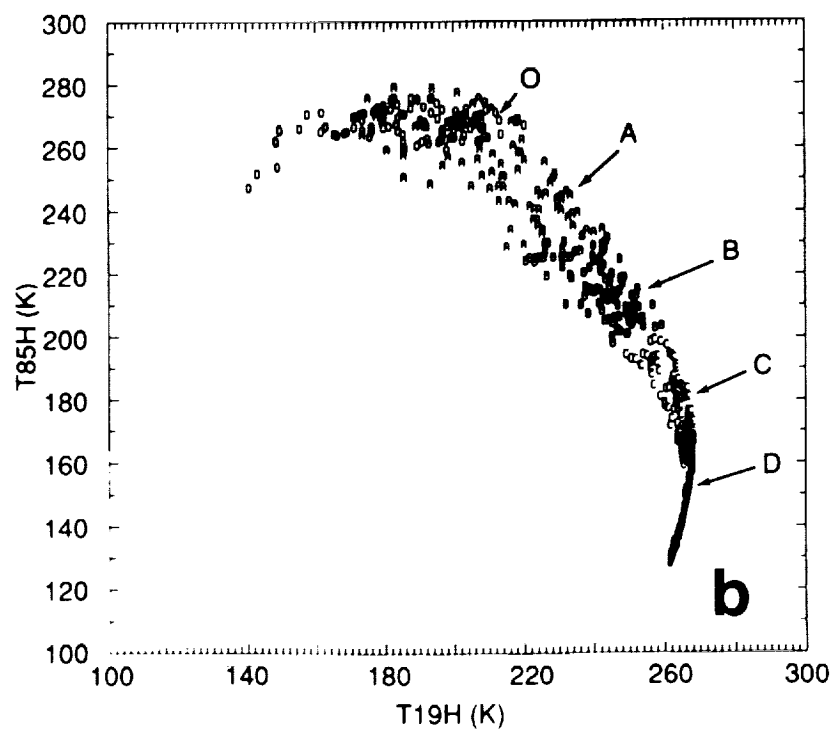
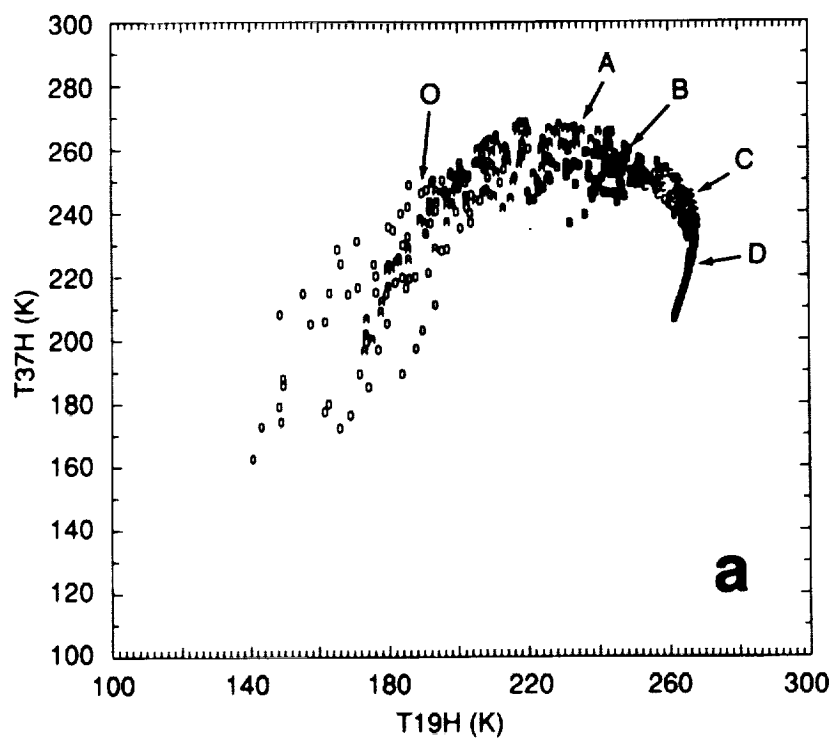


Figure 4. - Relationship between T_{19} , T_{37} , and T_{85} obtained from radiative transfer simulations. See Table 1 for information about the input data and the letters O, A, B, C, and D:
a) T_{19} vs. T_{37} ; b) T_{19} vs. T_{85} .

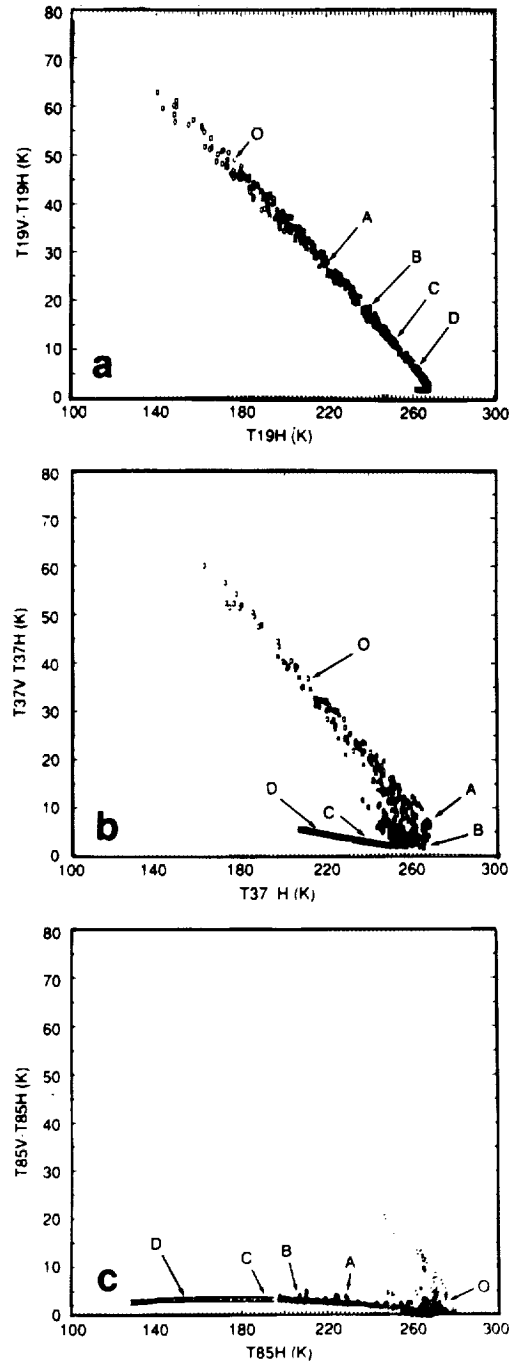


Figure 5. - Polarization effect ($T_V - T_H$) obtained from radiative transfer simulations. See Table 1 for information about the input data and the letters O, A, B, C, and D.

- a) $(T_V - T_H)$ vs. T_H at 19 GHz;
- b) $(T_V - T_H)$ vs. T_H at 37 GHz;
- c) $(T_V - T_H)$ vs. T_H at 85 GHz.

calculations is not necessarily realistic, and an arbitrary randomization does not account for the underlying correlations among the variables involved.

The nature of the simulated brightness temperatures as a function of rain rate may be explained as follows. Although there is scattering in all the layers of the atmosphere containing hydrometeors, cloud drops and rain drops below the freezing level mainly account for emission, while ice particles above the freezing level essentially contribute to scattering. The microwave radiometer looking down at a rain scene senses basically the warm emission of the rain and cloud layers that are below the freezing level. As this emission emerges through the frozen layers above, scattering decreases the brightness temperature. Since the effects of emission and scattering in the atmosphere occur jointly, identifying the source region of the radiation reaching the radiometer is difficult. Smith and Mugnai (1989) and Mugnai et al. (1990) have developed a theoretical framework for this problem requiring a coupled cloud radiation model.

In Fig. 4, a and b, the computed brightness temperatures T_{19} , T_{37} , and T_{85} in the horizontal polarization are compared using T_{19} as a common variable. The hydrometeor content pertaining to the data in these figures generally increases from left to right. The points on the extreme left of the figure have no rain, and as one moves along the cluster of data points to the right, the rain rate increases. Note that the data follow a significantly nonlinear course near the right

end, showing a decrease in brightness temperature in all channels as the rain rate increases.

The plot of T_{37} vs. T_{19} in Fig. 4, a, shows that initially both T_{19} and T_{37} increase as rain rate increases. At the point where $T_{37} = 270$ and $T_{19} = 220$ K (corresponding to a rain rate of about 3 mm/h) a peak in T_{37} is reached. For further increases in rain rate, T_{19} increases but T_{37} decreases, as the scattering from ice above the clouds strongly attenuates the radiation at 37 GHz. As stated earlier, ice scattering is much weaker at 19 GHz. When the rain rate reaches about 12 mm/h, T_{19} is about 270 K; above this rain rate, ice scattering decreases both T_{19} and T_{37} . Theoretical calculations made by Olson (1987) show a similar relationship between T_{18} and T_{37} . Further, Olson's calculations clearly show that because of weaker absorption and scattering properties at 6.6 and 10.7 GHz, the brightness temperatures at these low frequencies increase almost linearly up to a rain rate of at least 20 mm/h.

The plot of T_{85} vs. T_{19} in Fig. 4, b, shows basically that T_{85} is similar in character to T_{37} . However, both the rain absorption and ice-scattering effects are much more pronounced at 85 GHz. As a consequence, saturation at 85 GHz occurs at very low rain rates.

Based on these theoretical calculations, the polarization difference δ is examined for the microwave frequencies at 19, 37, and 85 GHz by plotting δ vs. T_H for each one of these channels in Fig. 5, a, b, and c. A salient feature of this figure is that the

polarization difference δ decreases almost linearly and approaches zero as T_H increases to about 270 K. Beyond that point, as the rain intensity increases further, $\delta = 0$, but T_H decreases markedly because of strong scattering. In Fig. 5 a-c, this physical mechanism manifests as a sharp turning point in T_H around 270 K. From the simulations shown here, one notes that this reversal in the 85-GHz channel starts at a very low rain rate ($R < 1$ mm/h), and, hence, most of the precipitation events show $\delta = 0$. Since at 37 GHz this reversal takes place at a much higher rain rate, fewer cases show the reversal. At 19 GHz, the number of these cases is further reduced.

It can be shown from simple theoretical considerations (see Appendix) that the initial linear relationship showing a decrease in δ as T_H increases can be accounted for by the growth in the effective rain area within the fov, provided that the scattering effects are negligible. The effective rain area is defined as the equivalent area, occupied by clouds and rain, that is capable of masking the surface. This means that in this area, the polarization effect produced by the surface is not observed by the radiometer. For instance, at 37 GHz, an area with about a 3-mm/h rain rate or clouds about 2 km thick with a liquid water content of about 1 g/m³ can mask the sea surface. Since rain and clouds coexist, suitable combinations of such hydrometeors can serve the same purpose.

c. Inferences

From the comparison of satellite measurements with those of the simulations, we arrive at some important conclusions. It should be borne in mind that the brightness temperature in the simulations is controlled by the prescribed spatial distributions of the hydrometeors, clouds, rain drops, and ice. These conclusions are

- i. The polarization effect, δ vs. T_H , based on observations as well as theory, can be accounted for in terms of the effective rain area in the fov, provided that the scattering effects are negligible. From the satellite observations, we find that at 18 or 19 GHz over the global oceans, the scattering effects are not discernable; at 37 GHz they are weak, while at 85 GHz they dominate.
- ii. The approximate linear relationship between brightness temperatures at 18 or 19 GHz and 37 GHz, observed by the satellite radiometers over the oceans, is not reproduced by the radiative transfer simulation model adopted here. This is because of inherent difficulties in defining realistic spatial distributions of rain and clouds in the model (a detailed explanation is given in the Appendix).
- iii. Scattering effects at 85 GHz can explain the negative slope between T_{85} and T_{19} observed in both the satellite and the simulated data. However, the satellite data show a much larger variability in T_{85} caused by scattering as compared to that in the simulations.

We observe from satellite data at frequencies $\nu \leq 37$ GHz that the emission effects produced by rain are dominating, while at 85 GHz, the scattering from ice above the rain clouds is important. The ice scattering and polarization is also dependent on the size and shape of the ice particles (Wu and Weinman, 1984). In the life cycle of rainstorms, the temporal and spatial distributions of rain and ice within the anvils are not necessarily closely correlated. Thus, in order to gain any rain information from 85-GHz data, we must first account for the ice effects. For these reasons, it is preferable to retrieve ocean rain data from absorption emission processes (see also Petty and Kataros, 1990).

In an earlier study (Prabhakara et al., 1986) the low-frequency SMMR measurements at 6.6 and 10.7 GHz were used to retrieve rain over oceans. At these low frequencies, the fov is large (more than 100 km). Also, the absorption is weak, which permits a linear approach. In this study, we are emphasizing the smaller fov (30 km) measurements at 37 GHz to obtain finer details in the rain patterns over the global oceans. Because of much stronger absorption at this frequency, the retrieval algorithm is expected to be nonlinear.

3. Spatial Distribution of Rain and Its Impact on Microwave Observations

Based on the satellite microwave data presented in Fig. 2, it is clear that the basic nature of the T_b 's at frequencies $\nu \leq 37$ GHz is such that to a first approximation they are all linearly related. However, the theoretical simulations adopted here cannot explain this approximate linear relationship between T_{19} and T_{37} . This linearity is apparently linked to the spatial distribution of rain as elaborated in the following discussion (see also the Appendix).

The GATE data (Chiu, 1988), the data from the FACE experiment (Lopez et al., 1989), and rain gauge measurements (Jones and Sims, 1978) show that the convective rain rates have frequency distributions that are highly nonlinear. This is because of the highly variable nature of rain in space and time. When the cumulative frequency of rain rate R is plotted against $\log R$, curves having the shape shown in Fig. 6 result. The shape of this curve may be explained by considering the role played by the vertical motions, i.e., updrafts in convective systems such as the Mesoscale Convective Systems (MCS). In such systems, there are a few tall convective towers developed by strong vertical updrafts, which produce heavy rain. The number of smaller convective clouds, associated with weaker updrafts and lighter rain, increases rapidly as their size decreases. It has been noted from observations and from theoretical simulations (Adler and Mack, 1984) that the heights of convective clouds tend to be linearly related to $\log R$. Apparently for these

reasons, the graphical relationship of the kind shown in Fig. 6 is produced.

The cumulative frequency distributions of the satellite brightness temperature measurements, presented on a linear scale, show a character similar to the corresponding distributions of $\log R$. To demonstrate this, frequency distributions have been constructed from the SSM/I 37-GHz data obtained over three oceanic regions (3° lat \times 5° long grid boxes) during July 1987. Two of these regions correspond to the rainy areas of the ITCZ and the midlatitudes that have been considered in Fig. 2. The third one is in the subsidence region near 30°N , 135°W . These distributions are shown in Fig. 7, a, b, and c. It should be remembered that the frequency distributions of rain rate, deduced from the rain-gauge data shown in Fig. 6, include only rain events and exclude rainless ones. On the other hand, distributions derived from satellite data, as shown in Fig. 7, a, b, and c, contain all events. If we wish to compare the statistics of rain gauges with those of satellites, we must exclude T_b values that do not correspond to rain.

Based on statistics of the satellite measurements, T_b 's that are less than a discriminant temperature T^* are excluded, where T^* can be the brightness temperature at the maximum in the frequency distribution. This procedure effectively truncates that portion of the T_b frequency distribution that does not correspond to rain events. When the cumulative frequency distributions of the remaining T_b 's

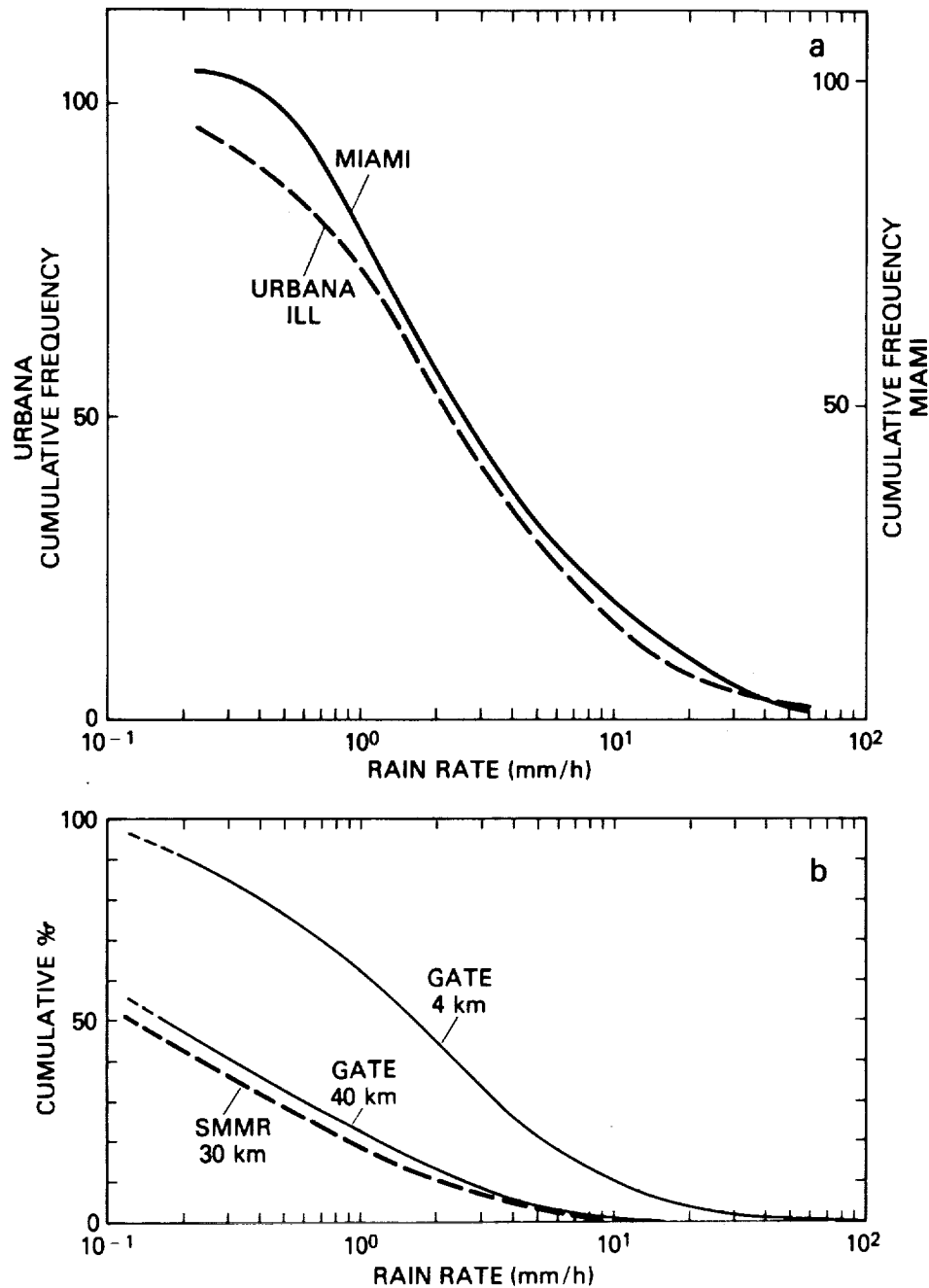


Figure 6.

- a) Cumulative frequency distribution of rain rates R (mm/h) vs. $\log R$ for Miami and Urbana based on 8 min rain gauge data presented by Jones and Sims (1978).
- b) Cumulative frequency distribution of rain rate R for GATE observations at $4 \times 4 \text{ km}^2$ and $40 \times 40 \text{ km}^2$ resolutions taken from the analysis of Chiu (1988). The distribution obtained from SMMR 37 GHz 30 km fov data is shown by a heavy dashed line for comparison.

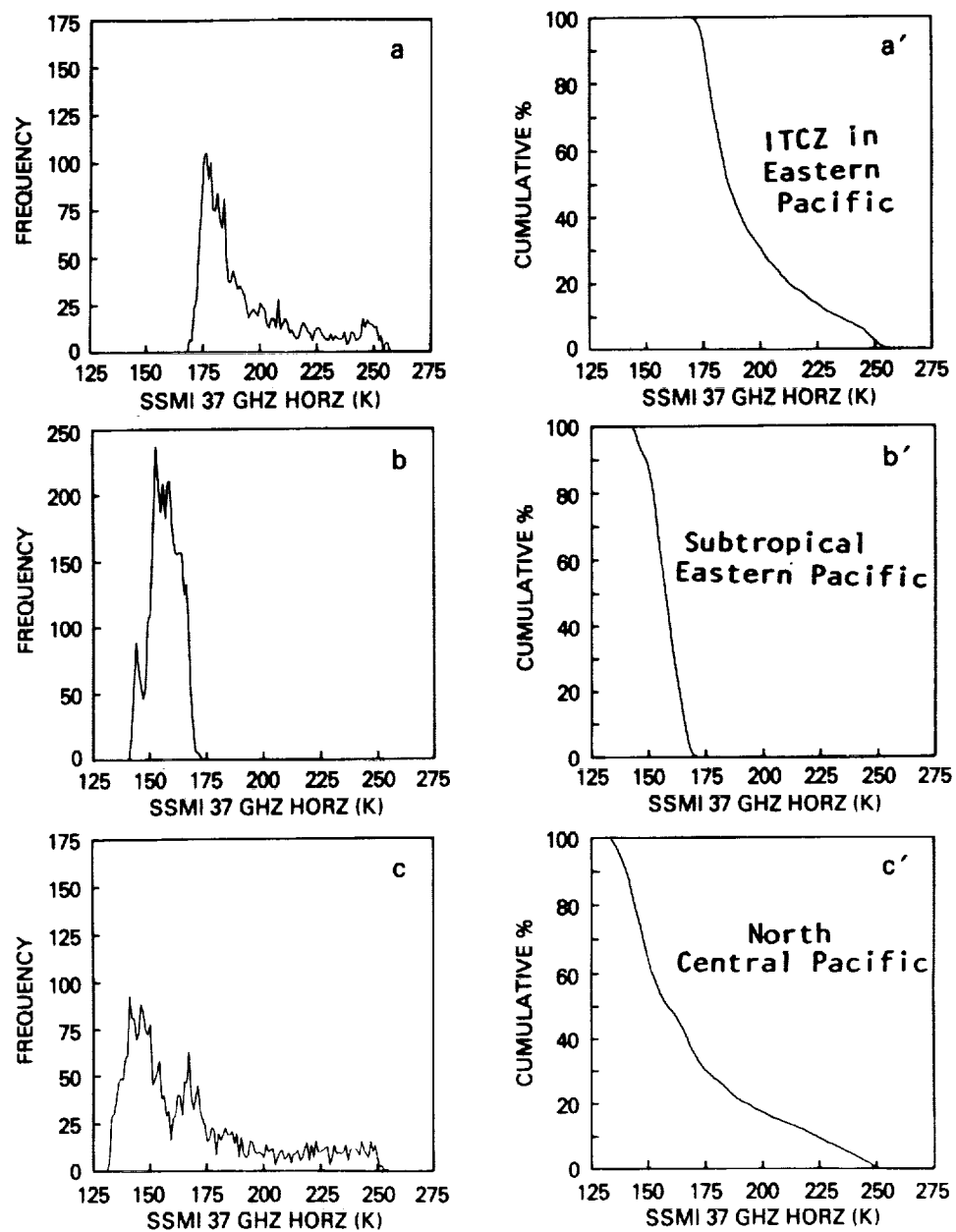


Figure 7. - Frequency distribution of SSM/I measured T_{37} in July 1987.

- a) $6^{\circ} - 9^{\circ}$ N, $90^{\circ} - 95^{\circ}$ W;
- b) $30^{\circ} - 33^{\circ}$ N, $135^{\circ} - 140^{\circ}$ W;
- c) $42^{\circ} - 45^{\circ}$ N, $160^{\circ} - 165^{\circ}$ W.

a', b', c' are the cumulative frequency distributions of T_{37} when rain is inferred.

are plotted as shown in Fig. 7, a', b', and c', the similarity between the cumulative frequency distributions resulting from rain-gauge log R analysis and those generated from the truncated satellite T_b 's becomes evident. The significance of T^* is clarified in Figs. 8 and 9. A precipitation event in the vicinity of Florida, which is characteristic of convectively active precipitation, is presented in Fig. 8, a. Contrasting with that, Fig. 9, a, shows a weak convective event near the Pacific coast of California, where large-scale subsidence inhibits the convective processes. One notices, from the T_{37} contours shown in these figures, that typically mesoscale convective systems having scales of about 100 km are excited in both places. In both cases, the frequency distribution of T_{37} , shown in Figs. 8, b, and 9, b, exhibits a maximum at a temperature that is about 15 K warmer than the lowest value of T_{37} in the distribution. The temperature at this maximum in frequency is denoted by T^* .

The largest T_{37} values in Figs. 8, a, and 9, a, correspond to the convective centers which occupy a small area (i.e., low frequency of observations), while the area under successively smaller T_{37} values increases radially outward from the centers (i.e., frequency increases), until the convective forcing vanishes near T^* , where there is a frequency maximum. At brightness temperature values less than T^* , clouds are apparently dissipating, eventually to reach undisturbed clear-sky conditions, i.e., minimum T_b over oceans. The area under undisturbed cloud-free sky is again small (i.e., low frequency). Thus, the satellite microwave observations strongly

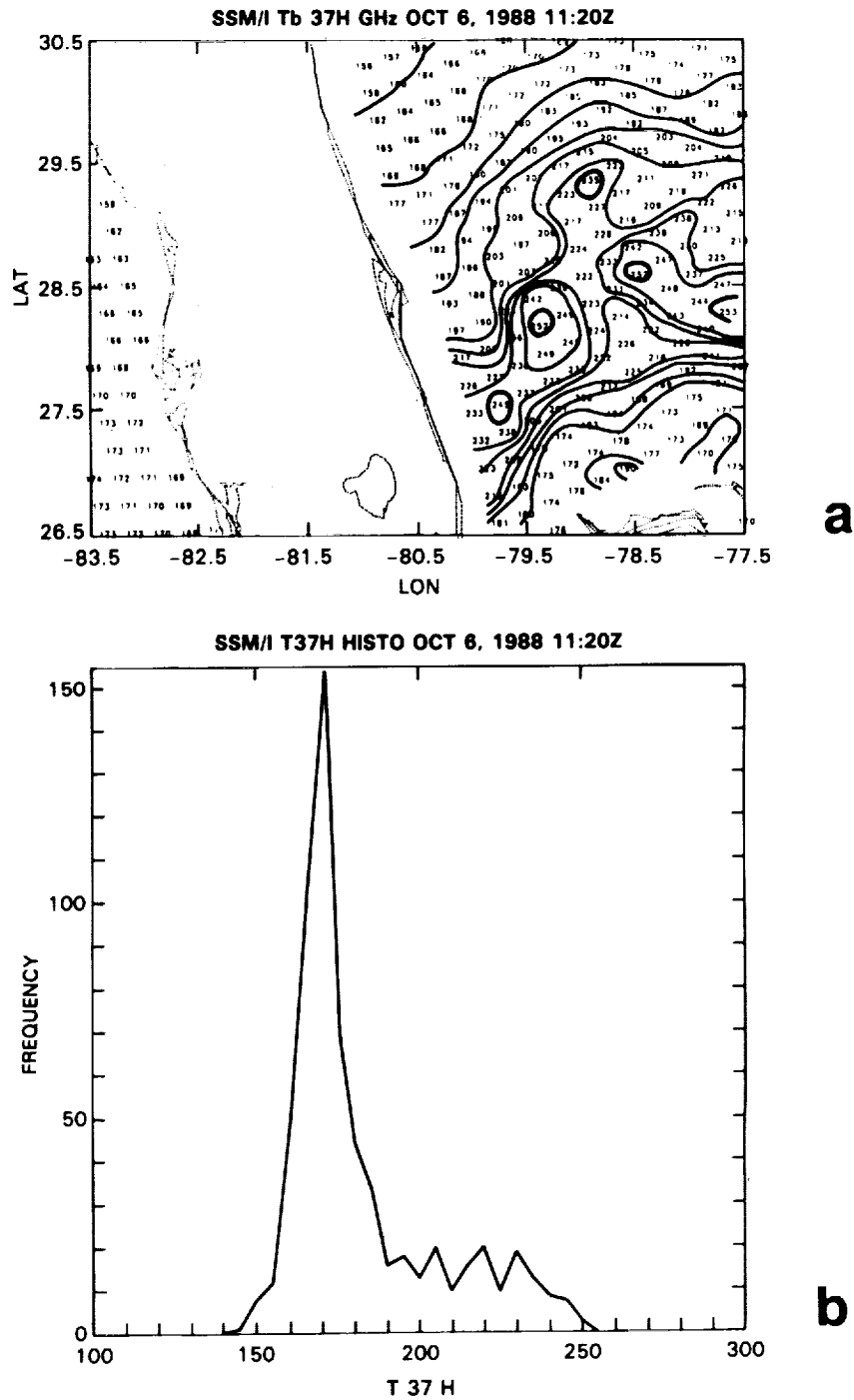


Figure 8.

- a) SSM/I T_{37H} contours identifying the mesoscale convective system (MCS) observed to the east of Florida over the Atlantic on Oct. 6, 1988. The MCS centers are identified with a heavy contour.
- b) Frequency distribution of T_{37H} shown above.

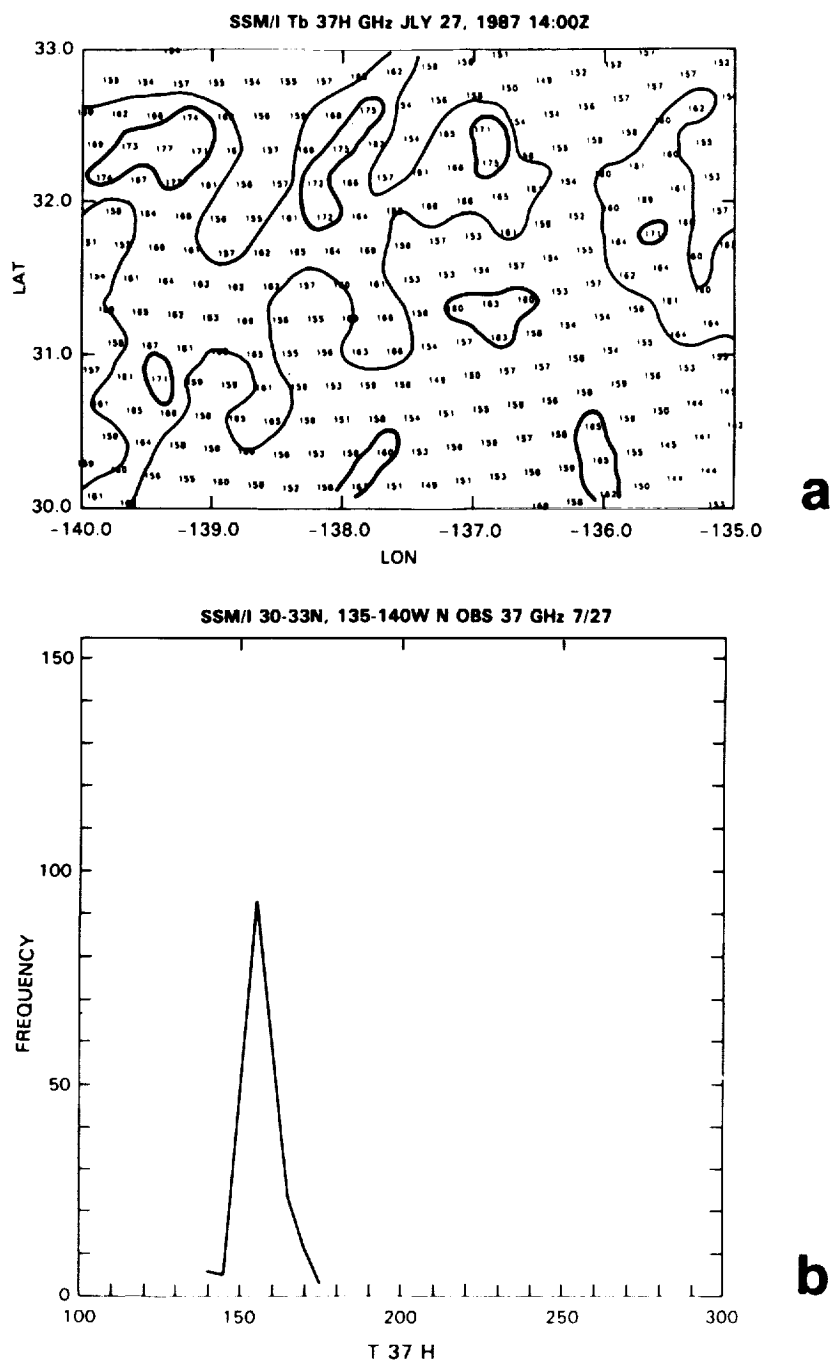


Figure 9.

- a) SSM/I T_{37H} contours identifying the mesoscale convective system (MCS) observed to the west of Baja California on July 27, 1987. The MCS centers are identified with a heavy contour.
- b) Frequency distribution of T_{37H} shown above.

suggest that the maximum in frequency at T^* is produced by the two competing forces, i.e., convective growth of clouds on one hand, and dissipation toward a cloud-free state on the other hand.

The microwave data could be scrutinized more intensively as a function of latitude to gain a better understanding of T^* . In Fig. 10, the SSM/I measurements during one month are used to generate the frequency distribution of T_{37} at each latitude, from 60°N to 60°S , along 145°W longitude. From this figure we notice that the minimum in T_{37} ($T_{37\text{min}}$) varies systematically from 60°N to 60°S . This minimum depends on the ocean temperature and on the water-vapor content in the atmosphere as a function of latitude. This dependence can be derived with the help of radiative transfer model calculations (Prabhakara et al., 1983) that utilize a large number of temperature and water-vapor profiles, observed by radiosondes at island stations that are spread over a wide latitudinal range from the Equator to 55°N . From such calculations, it can be shown that T_{37} in the absence of rain and clouds, i.e., $T_{37\text{min}}$, can be related to water vapor content w (g/cm^2) in the atmosphere by the following linear relationship:

$$T_{37\text{min}} = 126 + 6.8 w. \quad (1)$$

The $T_{37\text{min}}$ calculated here, including only water vapor and no clouds, corresponds to the $T_{37\text{min}}$ shown in Fig. 10.

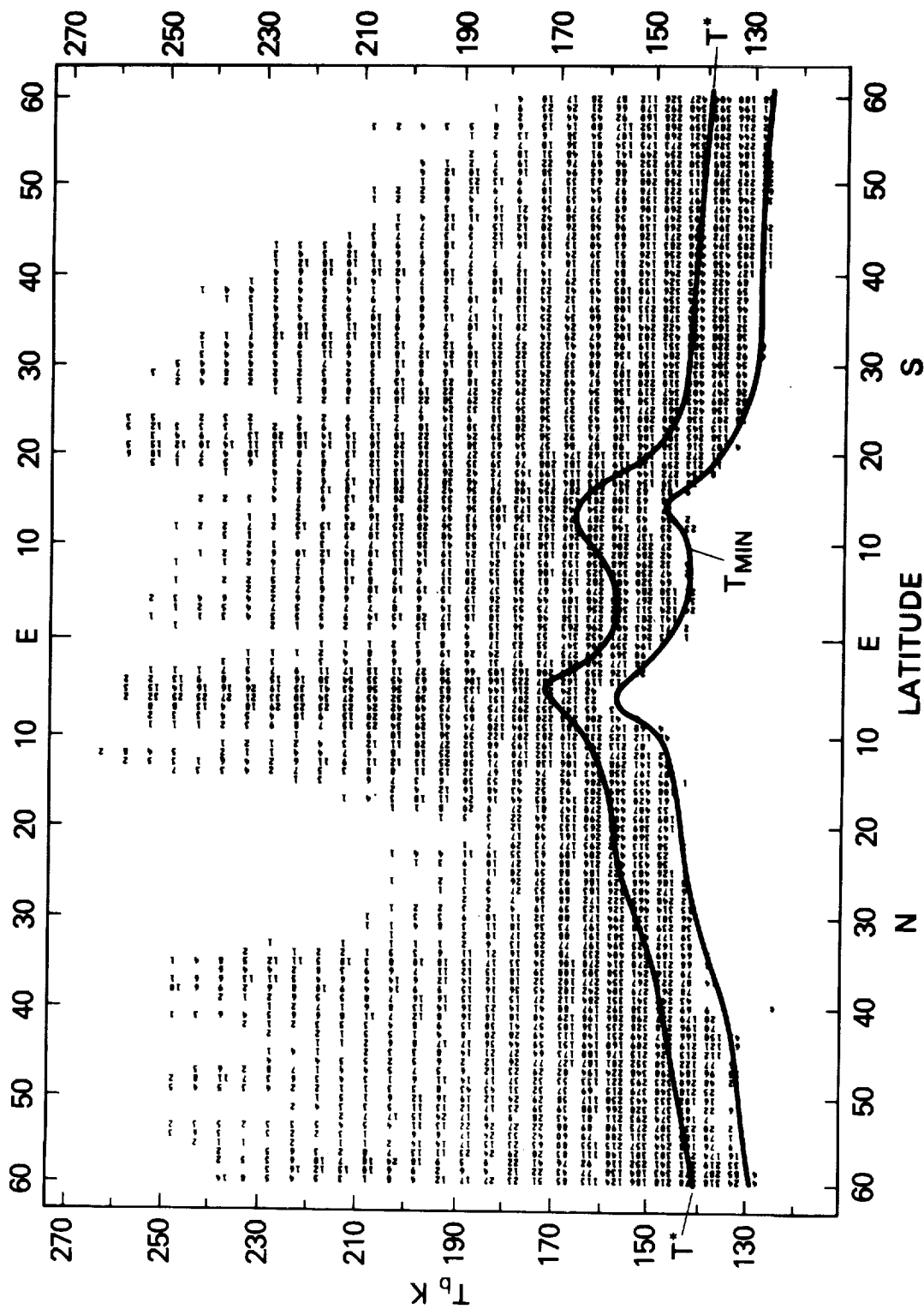


Figure 10. - Frequency distribution of T_{37} , in 5 K intervals, at each latitude from 60° N to 60° S at 145° W longitude constructed from SSM/I July 1987 data. $T_{37\text{min}}$ is the minimum brightness temperature and T^* is the brightness temperature at the maximum frequency in the distribution at each latitude.

Maximum frequency in the distributions shown in Fig. 10 occurs at a temperature denoted by T^* , which is about 15 K warmer than the minimum T_b at any given latitude. The value of T^* ranges from about 175 K in the highly convective tropical oceans to about 145 K in the high latitudes. The percentage of observations that fall in the interval from T_{37} minimum to T^* can be small, about 20%, in the rainy areas of the tropics and midlatitudes. In the dry subsidence areas, this fraction is substantially larger, often exceeding 50%. The statistical observations shown in Fig. 10 imply that at 37 GHz on the global oceans, T_{37} has to grow by about 15 K above the minimum in brightness temperature to allow for the development of rain-producing clouds.

These statistics of the logarithm of the rain rate R , composited from several storms and shown in Fig. 6, and of the satellite T_{37} , shown in Fig. 7, can be used to represent the spatial distribution of these variables for a single storm, provided that these statistics have the property of stationarity. When such stationarity exists, the percentage cumulative frequency distribution of $\log R$ represents the fractional area of the storm having a rain rate in excess of a given threshold (Chiu, 1988; Atlas et al., 1990a). Similarly, the percentage cumulative frequency distribution of T_b gives the fractional area of the storm in which T_b exceeds a given threshold. Hence, from the statistics of R and T_{37} , one can draw a correspondence between the spatial distributions of these two variables.

From the discussion presented here and in the Appendix we conclude that at 37 GHz, the channel used for rain retrievals, the convective dynamics that can produce a log-normal type of rain-rate distribution as shown in Fig. 6, play a strong role in modifying the brightness temperature and hence, this important effect has to be taken into account in retrieving rain rates.

4. Rain Retrieval Algorithm for the Oceans.

One important aspect of rain retrieval is the direct relationship between the T_{37} -GHz polarization difference δ_{37} and the T_{37} -GHz brightness temperature. An analysis of the data indicates that increasing the effective rain area in the radiometer's fov is responsible for the increase in T_{37} and a proportional decrease in δ_{37} (see Fig. 3 and Appendix). This basic result was emphasized in an earlier study (Prabhakara et al., 1989). In another study, Petty and Kastaros (1990) used simultaneous satellite and radar observations to arrive at the same conclusion, i.e., T_{37} and δ_{37} contain the same information. Thus in some sense, in our empirical approach with T_{37} as a basic parameter, we intrinsically account for the beam filling effects. However, this one piece of information is not sufficient to retrieve the distribution of rain over global oceans.

The minimum in T_{37} given by satellite microwave observations (Fig. 10) can be used to derive seasonal maps of columnar water-vapor content w in the atmosphere over oceans (Prabhakara et al., 1985). Water vapor is an essential ingredient in the precipitation mechanism. For this reason, the satellite derived w is included as a second piece of information in our rain-retrieval scheme. The discriminant brightness temperature T^* defined in section 3, is our third parameter. Note that w is given by Eq. (1), and T^* can be obtained over global oceans as a function of season from $T_{37\min}$, i.e., $T^* = T_{37\min} + 15$ (see Fig. 10). The two independent pieces of

information, T_{37} and $T_{37\min}$, yield the three parameters T_{37} , w , and T^* , which essentially determine our rain-retrieval scheme.

From the analysis of the rainfall data and the results of studies (Adler and Mack, 1984; Lopez et al., 1989), we can relate the effective rain area A to the logarithm of rain rate R . To satisfy the condition $R = 0$ for $A = 0$, we take

$$\log (R + 1) = a A, \quad (2)$$

where a is a constant greater than zero. From our interpretation of the analysis presented in Section 3, the area A also approaches zero for $T_{37} \rightarrow T^*$. Thus, we take a similar relationship associating A to $(T_{37} - T^*)$:

$$(T_{37} - T^*) = b A \quad (3)$$

where b also is a constant. From Eqs. (2) and (3) we have

$$\log (R + 1) = (T_{37} - T^*) a/b,$$

where a/b is constant for a given oceanic region. A more general form for this equation is

$$\log (R + 1) = (T_{37} - T^*)^{\lambda} a/b, \quad (4)$$

which allows for a possible nonlinear relationship between $\log R$ and $(T_{37} - T^*)$. The rain rate R is then given by

$$R = e[\beta(T_{37} - T^*)]^x - 1, \quad (5)$$

where β^x replaces a/b .

Eq. (5) constitutes the basic rain-rate retrieval algorithm. This equation indicates that precipitation does not happen in the area where T_{37} is less than T^* . Precipitation starts when the convective forcing is sufficient; and, in terms of the above mathematical formulation, this takes place when T_{37} is larger than T^* , i.e., T^* becomes a rain-no rain threshold. Note that this is not a required physical assumption.

For each grid box and time interval, we calculate $T_{37\min}$ and take $T^* = T_{37\min} + 15$. If we consider the cloud liquid-water content to be about 0.5 g/m^3 (Fletcher, 1966), then this 15-K growth in T_{37} corresponds to a columnar liquid-water content of 0.02 g/cm^2 , when the cloud is stratiform in nature and covers the entire fov with a thickness of 0.4 km. Similarly, if we consider cumuliform clouds 1 km thick covering 40% of the fov, the average columnar liquid-water content in the fov is again 0.02 g/cm^2 . These cloud liquid-water conditions associated with T^* appear to be the starting point of rain.

The functional form chosen allows for a nonlinear relationship between $\log R$ and $(T_b - T^*)$. Here, Eq. (5) is primarily meant to

describe the log-normal nature (see Fig. 6) of the rain-rate distributions. In this equation, when χ is equal to 1, R grows in a simple exponential way as a function of $\beta(T_b - T^*)$. However, when χ is larger than 1, R increases faster than the simple exponential for values of $\beta(T_b - T^*) > 1$, and decreases faster when $\beta(T_b - T^*) < 1$. Thus, with a knowledge of the frequency distribution of $(T_b - T^*)$ at a given place, Eq. (5) may be tuned with the help of the two constants β and χ to match the statistics of rain at that location.

In a global scale study of rain, we should be able to discriminate between stratiform rain vs. convective rain. Although both types of rain are present at all latitudes, convective rain contributes a larger fraction to the total rainfall, about 70% in the warm tropics (Houze and Betts, 1981; Houze and Hobbs, 1982). In the baroclinically active regions of the middle and high latitudes, as well as the subtropical regions of the oceans where large-scale atmospheric subsidence prevails, the fraction of the total rainfall arising from stratiform clouds is larger than that in the convective tropics. Since the microwave radiometer is sensing only the effective rain area, it is necessary to introduce into the rain algorithm a parameterization that can take into account the relative importance of convective vs. stratiform rain. This is done here empirically with the help of w . Basically, this parameterization asserts that the convective rain rate increases exponentially with w . As a result, in the region away from the water vapor-rich tropics, the convective rain rates decrease as water vapor decreases. The stratiform rain, which plays a significant role in these regimes, moderates this rapid

falloff to some extent. This parameterization is consistent with the fact that w decreases in the baroclinic zones of the middle and high latitudes, and also in the subtropical subsidence regions. Maps of satellite-derived w (see Prabhakara et al., 1985) reveal this.

Rain statistics over global oceans could vary regionally and as a function of season; this variability over the global oceans is modelled here in terms of the columnar water vapor content in the atmosphere. One may note that w is a function of seasonally varying sea surface temperature, and it also depends on the dynamical state of the atmosphere (Prabhakara et al., 1977). Taking advantage of these properties of w , the constant β in Eq. (5) is modified to be a parameter that increases with w . An additional parameter, $\gamma(w)$, which decreases with w , is introduced to incorporate the relative importance of convective vs. stratiform rain. With these parameters we have

$$R = \{ e^{[\beta(T_{37} - T^*)]^\chi} - 1 \} \gamma(w). \quad (6)$$

Basically, this parameterization asserts that the convective rain rate increases exponentially with w .

The dependence of β and γ on w , and the magnitude of the constant χ are determined by tuning Eq. (6) to match a) July rainfall statistics obtained in the GATE experiment over the tropical North Atlantic, and b) the summer rainfall climatology over the North

Atlantic developed by Dorman and Bourke (1981). We find $\chi = 1.7$, $\beta(w) = 0.012 + 0.003w$, and $\gamma(w) = 1.5 - 0.1w$ (w is given in g/cm^2).

The above formulation leads to a rapid decrease in rain rate R as $(T_b - T^*)$ and/or w decreases, as shown by the first term on the right-hand side of Eq. (6). The second term, which is linear in w , counteracts the first term to some extent. This second term represents, in an empirical way, enhancement of stratiform rain on global oceans as w decreases. It remains as a future research problem to verify the functional relationships used for $\beta(w)$ and $\gamma(w)$.

5. Application to Case Studies

Comparison of the rain rate statistics deduced from July 1974 GATE data (Hudlow and Patterson, 1979) with those of July 1979 SMMR T_{37} data is shown in Fig. 6, b. (Note that there was no El Niño event in either 1974 or 1979). In this figure, the GATE rain-rate statistics at 4- x 4-km² resolution, as well as the statistics of the same data averaged over a 40- x 40-km² area by Chiu (1988), are shown. The cumulative frequency distribution of rain rate derived from SMMR T_{37} data using Eq. (6), as shown in Fig. 6, b, agree reasonably well with the GATE 40- x 40-km² data. (Since some information in this channel is sensed over an area having a diameter larger than 30 km we are using GATE 40- x 40-km² statistics for comparison). In addition to this important statistical character of the rain, two more properties of the monthly rainfall; i.e., the monthly mean rain rate and the probability of rain occurrence in a month, are compared as follows.

The monthly mean rain rate \bar{R} is given by $\bar{R} = R'p$, where R' is the average rain rate obtained from the number of rain events n_R , which constitutes only a part of the total number of observations n . The probability p of rain occurrence in the GATE data is given by $p = n_R/n$. In the case of the satellite data, n_R is the number of SMMR observations when $T_{37} > T^*$ and n is the total number of observations.

The GATE July 1974 observed mean rain rate \bar{R} is 0.49 mm/h, and the \bar{R} for July 1979 obtained from SMMR is 0.55 mm/h. The probability p for GATE is 50%, while that for SMMR is 65%. This seems to suggest that a better match could be found with a different value of T^* (for example $T^* = T_{37\min} + 18$), but we have not attempted to fine tune beyond this level, because GATE data are from 1974 and the SMMR data are from 1979. Also note that SMMR observations are limited to local midnight and noon.

Table 2 is presented to show the dependence of R on T_{37} through the parameters β and γ that depend on w .

Table 2. - Rain Rate R (mm/h) Computed From Eq. (6) as a Function of T_{37}

w	T*	β	γ	R							
g/cm ²		x10 ⁻²		(T ₃₇)	170	190	210	230	250	255	260
1	148	1.5	1.4	0.24	0.83	2.03	4.49	9.78	11.9	14.6	
2	154	1.8	1.3	0.16	0.78	2.24	5.74	14.8	18.9	24.3	
3	161	2.1	1.2	0.07	0.63	2.20	6.56	20.2	27.1	36.8	
4	168	2.4	1.1	-	0.44	1.91	6.69	24.6	34.8	49.8	
5	175	2.7	1.0	-	0.24	1.48	6.08	26.6	39.5	59.6	

$$R = \{e^{[\beta(T_{37} - T^*)]^{1.7}} - 1\} \gamma(w)$$

The water-vapor-dependent variables T^* , β , and γ are listed. See text for a detailed explanation of β and γ .

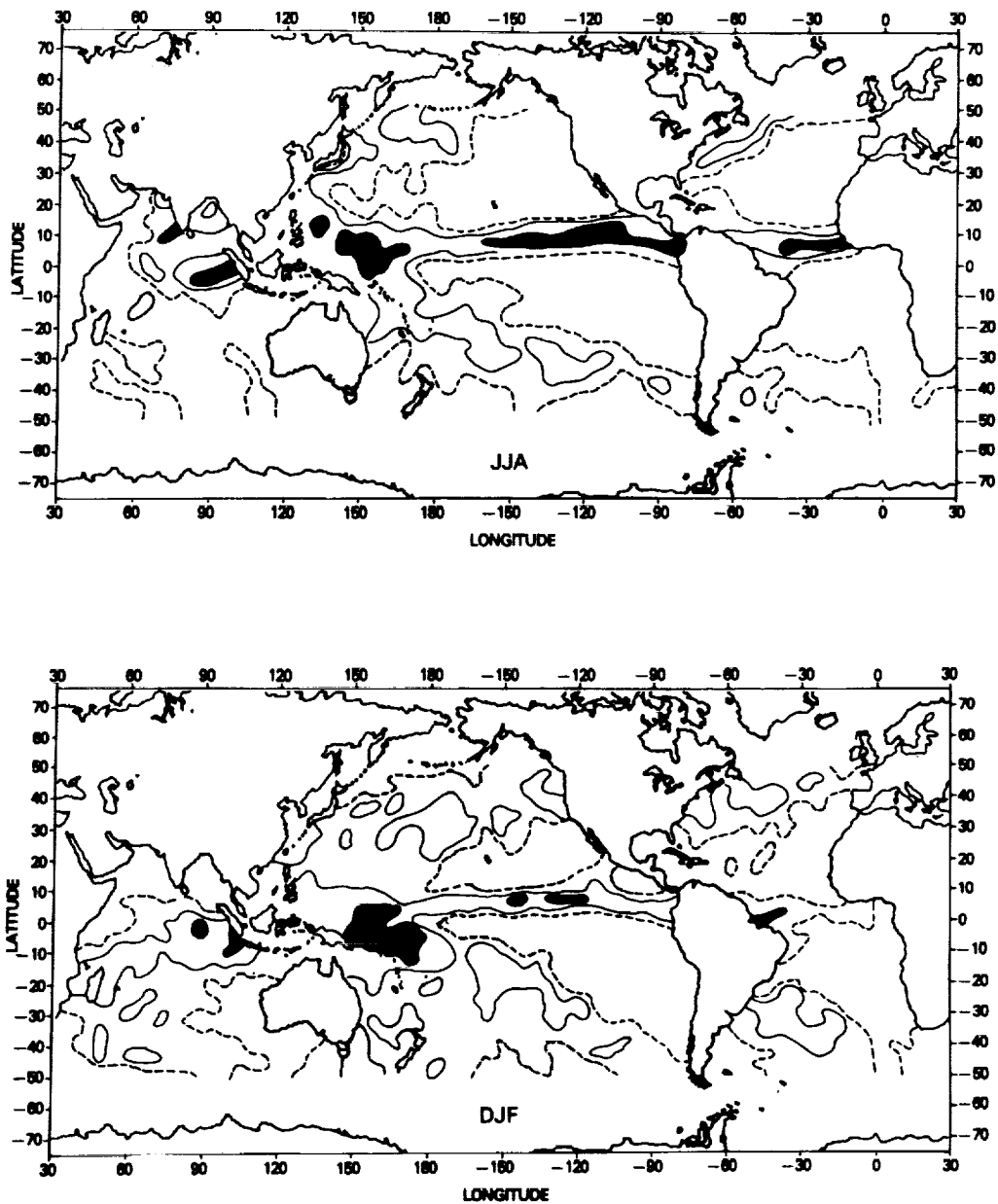


Figure 11. - Seasonal mean rain rate (mm/h) maps deduced from Nimbus 7 SMMR 37 GHz 30 km data between 50° N and 50° S for JJA (1979) and DJF (1979 and 1980). Contours are drawn at 0.1, 0.2, 0.4, 0.6 mm/h rain rates. The area with less than 0.1 mm/h is shaded lightly and that contour is shown by a broken line. Contours with values larger than 0.4 mm/h are shown by dark shading.

Seasonal mean rain rate maps over the oceans between 50°N and 50°S are shown in Fig. 11. These maps, derived from Eq. (6), utilize the SMMR T_{37} data of June, July, and Aug. 1979, and Dec. (79), Jan., and Feb. 1980. The rainfall patterns shown in the figure are in good agreement with the summer and winter maps of Dorman and Bourke (1979, 1981) (D&B, hereafter). Note that the D&B maps do not extend south beyond 30°S . Basically, this comparison suggests that the rain algorithm developed here can produce rainfall patterns on global oceans in accord with climatology. The significant features in those maps are the extremely low rain rate ($R \leq 0.05$ mm/h) in the subtropical eastern oceanic regions with subsidence and the extremely large rain rate $R = 0.6$ mm/h in the ITCZ. The warm ocean currents (Kuroshio and the Gulf Stream) reveal about 0.2 mm/h rain rate along their course in the midlatitudes. In addition, warm currents are associated with somewhat heavier precipitation rates in winter than in summer. The stratiform rain enhancement, incorporated into this algorithm with the parameter γ , has helped in obtaining satisfactory rain amounts in the midlatitudes in winter.

Besides comparing the seasonal mean rain maps of SMMR, we have also compared, separately for the Atlantic and Pacific Oceans, the zonally averaged rain rates for summer and winter derived from SMMR, with those of D&B in Fig. 12. This comparison shows the broad-based agreement in the tropics, subtropics, and midlatitudes.

The method presented here may be applied to satellite observations over the Atlantic Ocean to the east of Florida and the

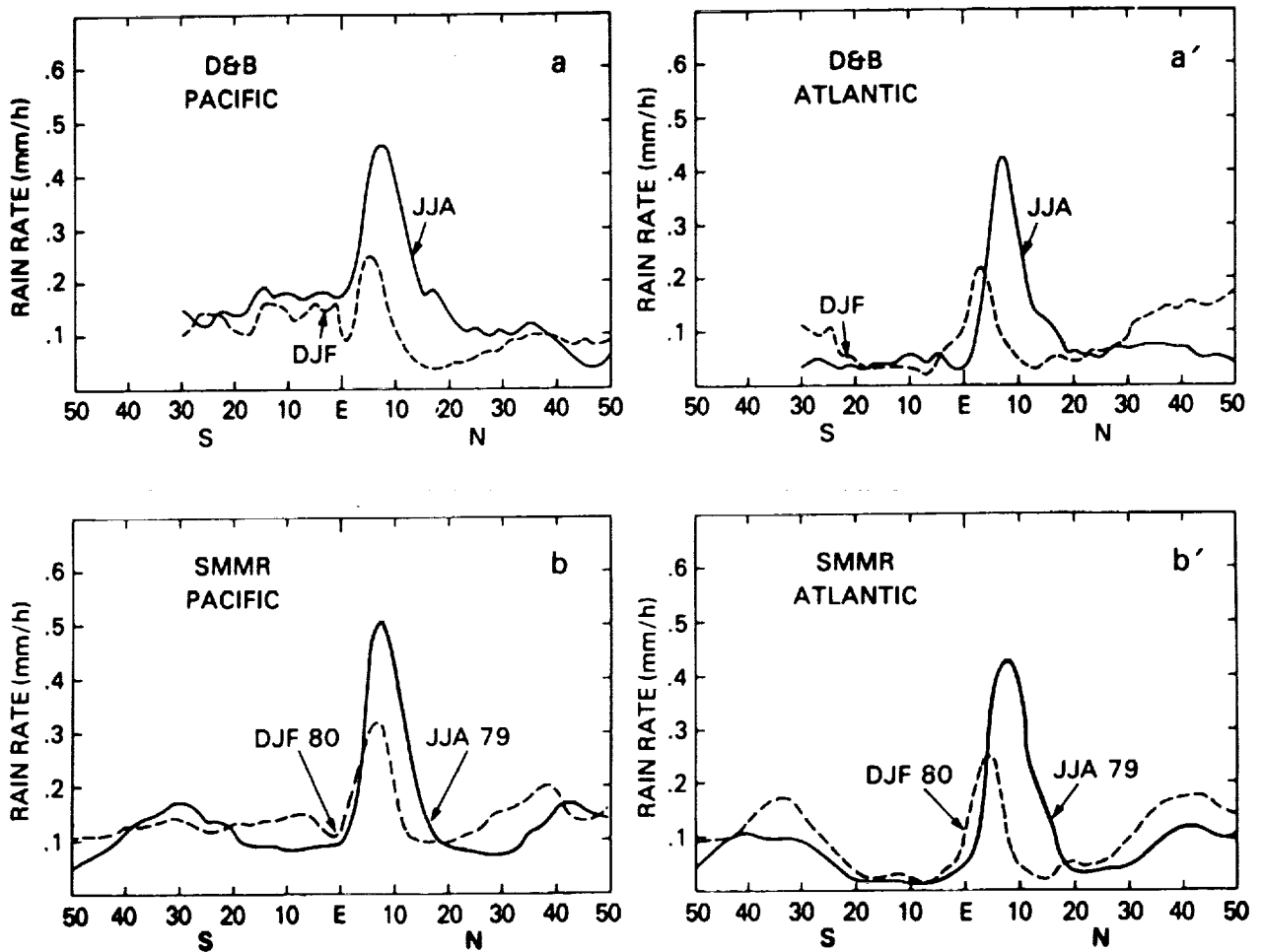


Figure 12. - Zonal mean rain rate (mm/h) for Pacific (a, b) and Atlantic (a', b') Oceans:
a & a' For summer and winter from Dorman and Bourke (1979, 1981)
b & b' SMMR JJA 1979, DJF 1980

retrieved rain rates could be compared with the results from the radar observations at Patrick Air Force Base, FL (28.5°N and 80.5°W). We find that treating the radar data, which is not calibrated against rain gauges, is fraught with problems (see Petty and Kastaros, 1990). Since reflectivity of precipitation normally decreases with height (except in cases of elevated bright band) and the observation height increases with range, average measured reflectivity for any fixed rain rate at the surface will decrease with range (Atlas et al., 1990b). The radar and the satellite radiometer are not sensing with similar spatial resolution. Thus, satellite-derived rain rate cannot be compared exactly with the radar measurements over a large area of about 250 x 250 km².

Recognizing these limitations, we display in Figs. 13a-13c the observations made by radar and SSM/I on three days: a) October 6, 1988, 1120 GMT, b) December 11, 1988, 2340 GMT, and c) January 25, 1988, 0004 GMT. The radar data at an elevation angle of 0.79 is shown on the left panel of each figure. The SSM/I 37-GHz horizontal channel data are shown on the right-hand panel. For simplicity, the radar data are contoured at four dBZ levels: 20, 25, 30, and, if needed, 35 dBZ. The largest contour that can be legibly displayed, 30 or 35 dBZ, includes all higher levels of reflectivity. The rain rates corresponding to the various dBZ levels are given in Table 3. It is apparent from radar data that the area occupied by a given rain rate decreases rapidly in size as the rain rate increases to larger values.

With regard to microwave data, we note that T^* changes from 170 K for the Oct. event to 158 K and to 156 K for the Dec. and Jan. events. The corresponding values of w deduced from Eq. (1) are 4.3, 2.55, and 2.25 g/cm², respectively. The rainfall patterns for the three cases, deduced from the SSM/I data using Eq. (6), are compared with the radar observations in Figs. 13a, 13b, and 13c. The SSM/I-derived rain patterns are similar to those of radar. However, SSM/I retrievals show a rain area larger than that given by radar. This is not surprising since, as explained earlier, radar leads to systematic underestimation of rain, depending on radar range. Also, the radar range itself is limited to about 250 km. These comparisons with the radar data show that the rainfall algorithm presented here is not only applicable to monthly mean statistics, but also holds well for individual cases.

Table 3. - Comparison of Rain Rate R (mm/h), for the Three Cases on the Atlantic to the East of Florida, With That Derived
a) From Patrick Air Force Base Radar Reflectivity in dBZ*,
and b) From SSM/I Observed T_{37} (K) Using Eq. (6)

dBZ	R (mm/h)	T_{37}		
		Oct. 88 ($T^* = 170$ K)	Dec. 88 ($T^* = 158$ K)	Jan. 88 ($T^* = 156$ K)
20	0.5	192	184	184
25	1.3	203	200	200
30	3.2	218	217	217
35	8.1	232	236	237
38	14.1	242	246	248
40	20.3	247	255	259

* $\text{dBZ} = 10 \log_{10} Z$

$Z = 230 R^{1.25}$

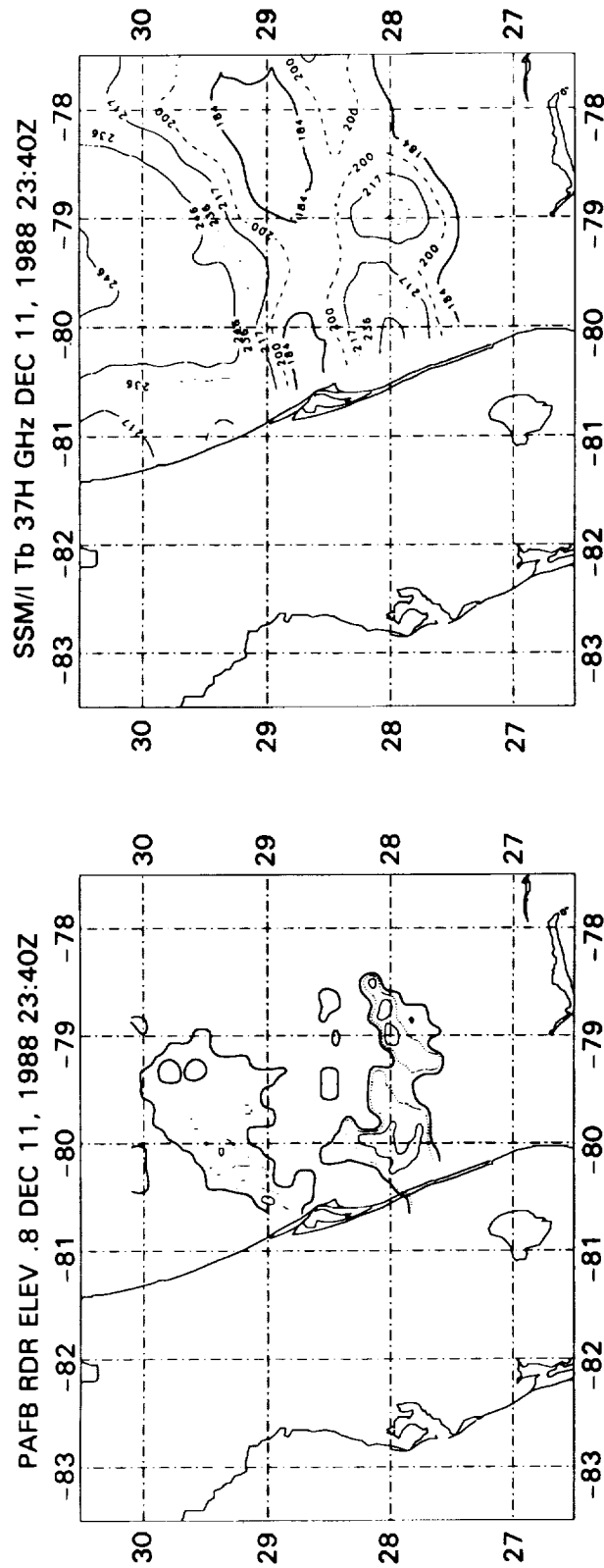


Figure 13a.

Left panel: Radar reflectivity measurements from Patrick Air Force Base (28.5° N and 80.5° W). Reflectivity at four successive levels, spanning 20 to 35 dBZ, are contoured. Outermost contour is 20 dBZ. Innermost contour includes all levels above 35 dBZ.

Right Panel: SSM/I T_{37} brightness temperature measurements, contoured at five successive levels spanning 192 to 242 K, are shown.

See Table 3 for a correspondence between reflectivity, rain rate, and brightness temperature.

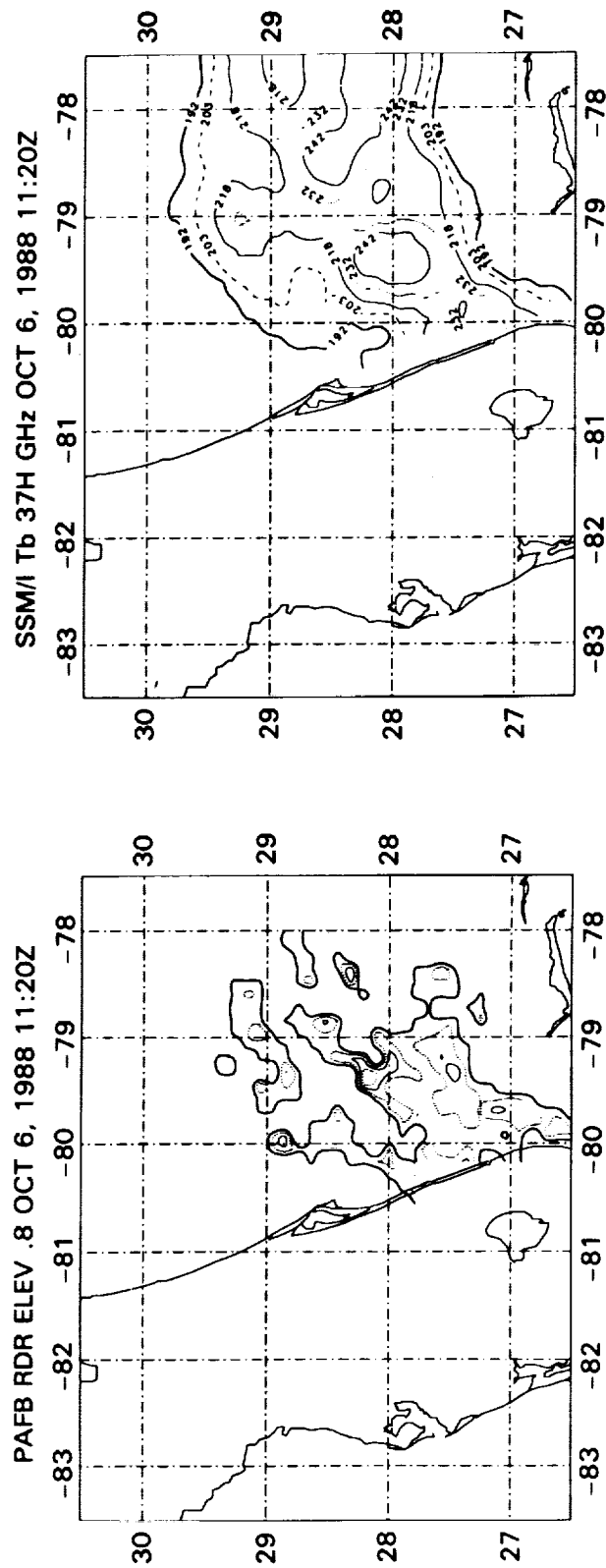


Figure 13b.

Left panel: Radar reflectivity measurements from Patrick Air Force Base. Reflectivity at three successive levels spanning 20 to 30 dBZ are contoured. Outermost contour is 20 dBZ. Innermost contour includes all levels above 30 dBZ.

Right Panel: SSM/I T_{37} brightness temperature measurements, contoured at five successive levels spanning 184 to 246 K, are shown.

See Table 3 for a correspondence between reflectivity, rain rate, and brightness temperature.

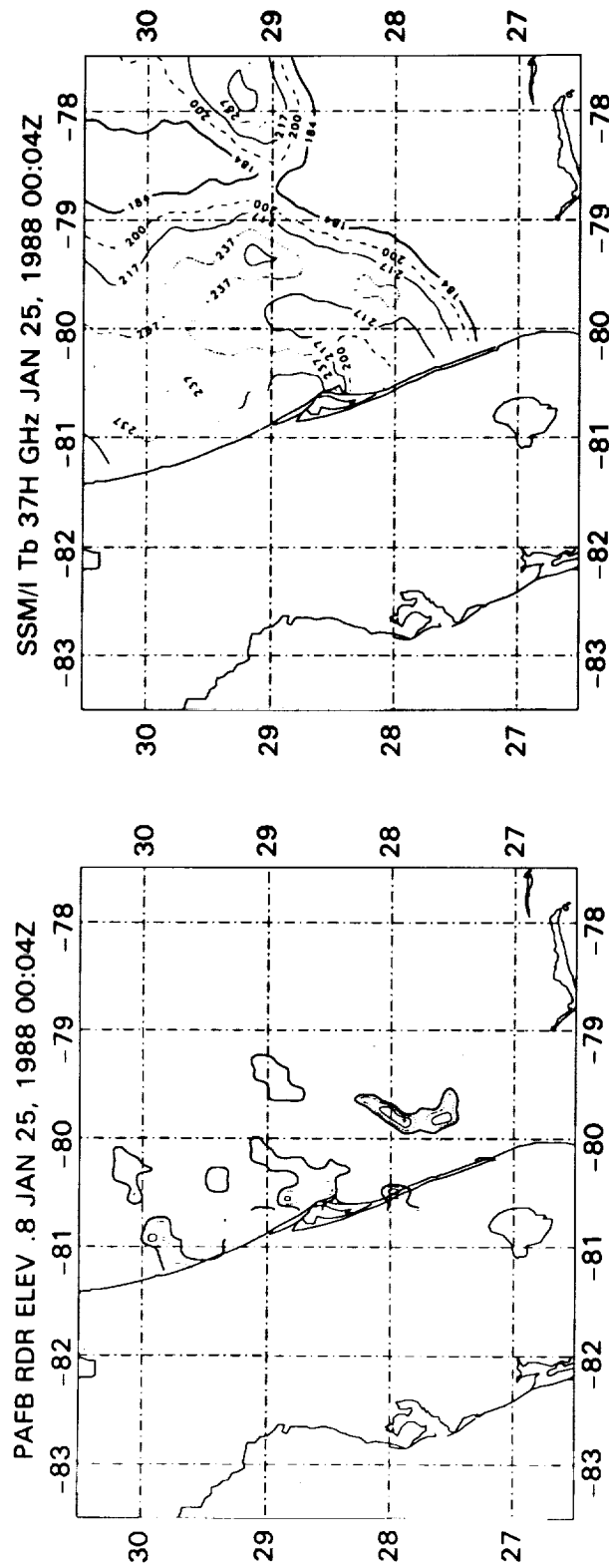


Figure 13c.

Left panel: Radar reflectivity measurements from Patrick Air Force Base. Reflectivity at three successive levels spanning 20 to 30 dBZ are contoured. Outermost contour is 20 dBZ. Innermost contour includes all levels above 30 dBZ.

Right Panel: SSM/I T_{37} brightness temperature measurements, contoured at five successive levels spanning 186 to 248 K, are shown.

See Table 3 for a correspondence between reflectivity, rain rate, and brightness temperature.

6. Discussion and Conclusion

The highly variable nature of rain in space and time is produced by the convective updrafts that result from the convergence and condensation of water vapor. These updrafts determine the height of the rain clouds and the drop-size distribution in the rain coming from these clouds. As a result of these complex dynamical and thermodynamic processes, horizontally inhomogeneous distributions in the liquid water content and drop size are produced. The microwave radiometer, with an fov that is large compared to individual rain cells, is responding to some area-averaged properties of these variables. The present study makes use of the detailed observational and theoretically inferred properties of the rain cells to develop an empirical relationship between the radiometric brightness temperature and the rain rate.

The radiometer response is not directly proportional to the amount of emitting matter (liquid drops) in the fov because of the saturation effects. The response, T_b , is apparently dependent on the effective area occupied by the emitting hydrometeors (Prabhakara et al., 1989; Petty and Kassaros, 1990). The water vapor content in the atmosphere constitutes a link between this effective area and the rain rate.

The microwave measurements from SMMR and SSM/I contain one strong piece of information related to the rain emission. The

same measurements can indicate the columnar water vapor content w in the absence of clouds and rain. Information in addition to T_b and w is needed in order to retrieve rainfall over the oceans. Thus, an empirical parameter T^* is introduced to indicate the start of rain, this T^* is deduced from the spatial and temporal variations in the T_{37} data. The relative magnitudes of stratiform vs. cumuliform rain are parameterized with the help of w .

The 85-GHz measurements show an independent character when compared to those of low-frequency measurements. As discussed earlier, this independent character is largely due to scattering by ice above the rain clouds. The temporal and spatial evolution of ice above the rain clouds, and the shape and size of ice particles are relevant in explaining the 85-GHz brightness temperature and polarization effects. At present, we do not have enough observational information about ice, such as the rain gauge statistics or GATE data, to develop a suitable theoretical or empirical model and to relate it to rain.

This rain estimation technique is not tested in detail with ground truth over widely different oceanic regions of the globe. The single test over the GATE region demonstrates the feasibility of matching reasonably well the frequency distribution of rain rate, the monthly mean, and the probability of rain occurrence with those obtained from satellite data. The technique can apparently reproduce the gross characteristics of the large-scale and seasonal variations of rainfall over oceans.

There are, however, several limitations to the rain-retrieval method developed here. One cannot partition satisfactorily the liquid water contained in the rain and clouds (Smith and Mugnai, 1988); the horizontal and vertical dimensions of the rain cells are unknown; the rain-column height and the drop-size distribution are not explicitly known; the effect of scattering by ice on top of the rain clouds is not taken into account; the sea surface emissivity changes due to wind are ignored. These unresolved variables will manifest as errors in the rain estimation. Space-borne radar measurements could improve the situation significantly and help to get better rain retrievals.

When good ground-truth information on hydrometeors and surface conditions is available, it may be possible to take advantage of the weak independent information at frequencies $\nu \leq 37$ GHz, present in the microwave measurements to refine the rain-retrieval method. Multifrequency measurements made with one fov would be best suited for this purpose because of the highly inhomogeneous nature of rain.

Finally, let us consider the VIS/IR rain estimates vs. the microwave method. Over the oceans, the basic difference between IR vs. microwave measurement is that in the IR, for most of the clouds, both the cloud height and its fractional cover in the fov are influencing the brightness temperature measured at the top. On the other hand, we find that the microwave SMMR or SSM/I data are more specific to rain. The effective rain area over the oceans is the

dominant information at frequencies $\nu \leq 37$ GHz, when the fov is 30 km or larger. However, there are common problems such as discriminating the convective rain vs. stratiform rain (see, for example, Adler and Negri, 1988).

Because of the nature of the response to cloud amount and height in the IR, the frequency distribution of brightness temperature in the IR is generally like the inverted letter "U" with a very broad maximum. On the other hand, we find a relatively sharp peak near low values of T_b in the frequency distribution of the microwave, and a long tail with marked decay toward the warm T_b .

Based on this study, we conclude that the passive microwave radiometer with an fov of about 30 km, at a frequency $\nu \leq 37$ GHz, can give useful rain information over global oceans. The addition of an IR radiometer with a fine fov could reveal the cloud-height variability within the fov of the microwave radiometer. This information may help improve the rain retrievals. In the TRMM experiment, it will be possible to exploit the combined capabilities of the IR and microwave radiometers.

Appendix

Effective Rain Area

When the scattering effects in the field of view (fov) of the radiometer are negligibly small, the radiative transfer in the microwave region may be used to relate the brightness temperature T_b measured at the top of the atmosphere to the atmospheric variables as follows (e.g., Chang and Wilheit, 1979):

$$T_b = T_s \epsilon_s \tau_s + \int T(p) d\tau(p) + (1 - \epsilon_s) \tau_s \int T(p) d\tau'(p), \quad (A.1)$$

where

- T_s is the surface temperature;
- ϵ_s is the surface emissivity;
- p is the pressure in the atmosphere;
- $\tau(p)$ is the transmission of the atmosphere from any level p to the top of the atmosphere. This includes the effect of all attenuating ingredients in the atmosphere;
- τ_s is the transmission from the surface to the top of the atmosphere;
- $\tau'(p)$ is the transmission from any level p to the surface.

The above equation may be simplified as

$$T_b = \underbrace{T_s \epsilon_s \tau_s}_I + \underbrace{\bar{T}_1 (1 - \tau_s)}_{II} + \underbrace{\bar{T}_2 (1 - \epsilon_s) \tau_s (1 - \tau_s)}_{III}, \quad (A.2)$$

where \bar{T}_1 and \bar{T}_2 are the equivalent radiative temperatures of the atmosphere for the upwelling and downwelling radiation (Prabhakara et al., 1983).

In the above equation, the term I represents the emission from the surface emerging from the atmosphere. The term II represents the atmospheric emission to space, and term III represents the radiation reflected by the surface and then transmitted to the top of the atmosphere.

Equation (A.2) may be rewritten as

$$T_b = \epsilon_s \tau_s [T_s - \bar{T}_2 (1 - \tau_s)] + (\bar{T}_1 + \bar{T}_2 \tau_s) (1 - \tau_s). \quad (A.3)$$

This equation shows that as τ_s approaches zero, T_b approaches \bar{T}_1 . Then no radiation from the surface reaches the top of the atmosphere, and so no polarization effects from the surface will be noticed, i.e., $(T_V - T_H) \approx 0$. We expect this when there are optically thick rain and clouds covering the entire fov of the instrument. This is apparent in the satellite-measured 37-GHz data when $T_{37} \approx 260$ K (Fig. 3, b). Thus, we assume that when the rain and clouds are optically thick, the effective emission temperature $T_c \equiv \bar{T}_2$, which is about 260 K.

Now let us assume that the fov is partially covered by optically thick rain and clouds, and the effective fractional area occupied by these hydrometeors is A_e . The remaining fraction $(1 - A_e)$ is then

free of rain clouds over the ocean. In this rain-free area, τ_s is substantially greater than zero. The brightness temperature T_b in the fov corresponding to this situation is given by

$$T_b = T_{\text{open}} (1 - A_e) + T_c A_e, \quad (\text{A.4})$$

where T_{open} in the first term on the right-hand side represents the brightness temperature in the rain-free area.

From Eq. (A.3), we note that as $\tau_s \rightarrow 1$, $T_b = T_{\text{open}} \rightarrow \epsilon_s T_s$. Substituting this approximation for T_{open} in Eq. (A.4) we have

$$\begin{aligned} T_b &\approx \epsilon_s T_s (1 - A_e) + T_c A_e \\ &\approx \epsilon_s T_s + A_e (T_c - \epsilon_s T_s). \end{aligned} \quad (\text{A.5})$$

As a result we have

$$\begin{aligned} T_v &\approx \epsilon_v T_s (1 - A_e) + T_c A_e \\ T_H &\approx \epsilon_H T_s (1 - A_e) + T_c A_e \\ (T_v - T_H) &\approx (\epsilon_v - \epsilon_H) (1 - A_e) T_s, \end{aligned} \quad (\text{A.6})$$

where ϵ_v and ϵ_H are the emissivities of the sea surface applicable to the horizontal and vertical components.

From Eq. (A.6), it follows that

$$\begin{aligned} \text{when } A_e \approx 1, \quad T_H &\equiv T_c \equiv 260 \text{ K} \quad \text{and } (T_V - T_H) \approx 0 \\ \text{when } A_e \approx 0, \quad T_H &\equiv \epsilon_H T_s \quad \text{and } (T_V - T_H) \approx (\epsilon_V - \epsilon_H) T_s. \end{aligned}$$

This reasoning explains the connection between the effective rain area A_e and the polarization information shown in Figs. 3 and 5.

Obviously the equations shown here will not be valid in the presence of scattering effects of the hydrometeors. The above analysis also leads us to infer that the effective area A_e , in which the opacity of rain and clouds is sufficiently large, is directly related to T_b measured by a radiometer.

In addition, a plot of the SSM/I-observed polarization difference $\delta (= T_V - T_H)$ at 19 vs. δ at 37 GHz, as shown in Fig. A1, a and b, gives a better understanding of the effective rain and cloud areas; i.e., these two channels are linearly related to one another except when the 37-GHz channel saturates. This explains the linear relationship between T_{19} and T_{37} observed in the satellite data (Fig. 2, a and b). Simulations (Fig. 3, a) could not show this linear relationship between T_{19} and T_{37} , because in such calculations, the spatial distribution of the hydrometeors in the fov is not specified in a realistic way.

We conclude from this discussion that the spatial distribution of rain and clouds profoundly influences the microwave radiometer

observations at frequencies $\nu \leq 37$ GHz and forces them to be linearly related to one another over a wide range of rain conditions.

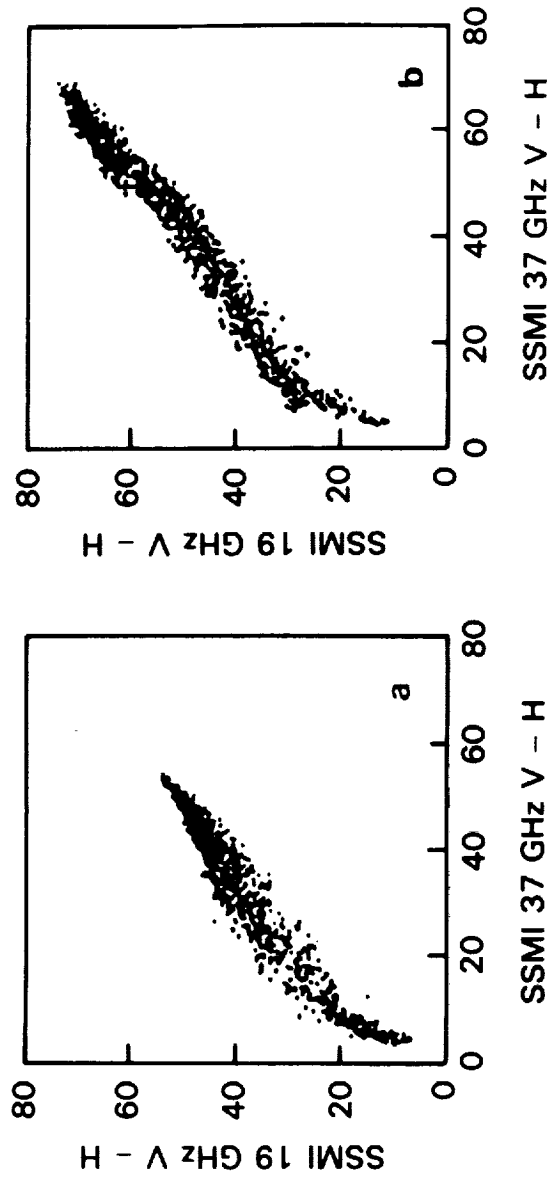


Figure A1. - Comparison of SSM/I observed polarization difference ($T_V - T_H$) at 19 and 37 GHz:
a) In the ITCZ region of the Eastern Pacific ($6^\circ - 9^\circ$ N and $90^\circ - 95^\circ$ W) during July 1987;
b) In the North Central Pacific ($42^\circ - 45^\circ$ N and $160^\circ - 165^\circ$ W) during July 1987.

References

- Adler, R. F., and A. J. Negri, 1988. A Satellite Infrared Technique to Estimate Tropical Convective and Stratiform Rainfall. J. Appl. Meteor., vol. 27, pp. 30-51.
- Adler, R. F., and R. A. Mack, 1984. Thunderstorm Cloud Height-Rainfall Rate Relations for Use With Satellite Rainfall Estimation Techniques. J. Climate Appl. Meteor., vol. 23, pp. 280-296.
- Arkin, P. A., 1979. Relationship Between Fractional Coverage of High Cloud and Rainfall Accumulations During GATE Over 'B' Scale Array. Mon. Wea. Rev., vol. 107, pp. 1382-1387.
- Arkin, P. A., and B. N. Meisner, 1987. The Relationship Between Large-Scale Convective Rainfall and Cold Cloud Over the Western Hemisphere During 1982-1984. Mon. Wea. Rev., vol. 115, pp. 51-74.
- Atlas, D., D. Rosenfeld, and D. A. Short, 1990a. The Estimation of Convective Rainfall by Area Integral. Part I. The Theoretical and Empirical Basis. J. Geophys. Res., vol. 95, pp. 2153-2160.
- Atlas, D., D. Rosenfeld, and D. B. Wolff, 1990b. Climatologically Tuned Reflectivity-Rain Rate Relations and Links to Area-Time Integrals. J. Appl. Meteor., vol. 29, pp. 1120-1135.
- Chang, A. T. C., and T. T. Wilheit, 1979. Remote Sensing of Atmospheric Water Vapor, Liquid Water and Wind Speed at the Ocean Surface by Passive Microwave Techniques From Nimbus 5 Satellite. Radio Sci., vol. 14, pp. 793-803.
- Chiu, L. S., 1988. Estimation of Areal Rainfall from Rain Area. Proceedings, International Symposium on Tropical Precipitation Measurements, Tropical Rainfall Measurements, J. S. Theon and N. Fugono, eds. A. Deepak Publishing, Hampton, VA, pp. 361-368.

- Doneaud, A. A., S. Ionescu-Niscov, D. L. Priegnitz, and P. L. Smith, 1984. The Area Time Integral as an Indicator for Convective Rain Volume. J. Climate Appl. Meteor., vol. 23, pp. 555-561.
- Dorman, C. E., and R. H. Bourke, 1979. Precipitation Over the Pacific Ocean, 30° S to 60° N. Mon. Wea. Rev., vol. 107, pp. 896-910.
- Dorman, C. E., and R. H. Bourke, 1981. Precipitation Over the Atlantic Ocean, 30° S to 70° N. Mon. Wea. Rev., vol. 109, pp. 554-563.
- Fletcher, N. H., 1966: The Physics of Rainclouds. Cambridge University Press.
- Gloersen, P., and L. Hardis, 1978. Scanning Multichannel Microwave Radiometer (SMMR) Experiment. Nimbus 7 User's Guide. Edited by C.R. Madris. NASA/GSFC, Greenbelt, MD, pp. 213-245.
- Hollinger, J., R. C. Lo, G. Poe, R. Savage, and J. Pierce, 1987. Special Sensor Microwave/Imager User's Guide. Naval Research Laboratory, Washington, D.C., 120 pp.
- Houze, R. A., and A. K. Betts, 1981. Convection in GATE. Rev. Geophys. and Space Phys., vol. 41, pp. 541-576.
- Houze, R. A., and P. V. Hobbs, 1982. Organization and Structure of Precipitating Cloud Systems. Advances in Geophysics, vol. 24, pp. 225-315.
- Hudlow, M. D., and V. L. Patterson, 1979. GATE Radar Rainfall Atlas. NOAA Special Report, U.S.G.P.O., Washington, D.C.
- Jones, D. M. A., and A. L. Sims, 1978. Climatology of Instantaneous Rainfall Rates. J. Appl. Meteor., vol. 17, pp. 1135-1140.
- Kilonsky, B. J., and C. S. Ramage, 1975. A Technique for Estimating Tropical Open Ocean Rainfall from Satellite Observations. J. Appl. Meteor., vol. 15, pp. 972-975.
- Kummerow, C., R. A. Mack, and I. M. Hakkarinen, 1989. A Self-consistency Approach to Improve Microwave Rainfall Estimation From Space. J. Appl. Meteor., vol. 28, pp. 869-884.

- Lau, K-M., and P. H. Chan, 1988. Intraseasonal and Interannual Variations of Tropical Convection: A Possible Link Between the 40-50 Day Oscillation and ENSO? J. Atmos. Sci., vol. 45, pp. 506-521.
- Lopez, R. E., D. Atlas, D. Rosenfeld, J. L. Thomas, D. O. Blanchard, and R. L. Holle, 1989. Estimation of Rainfall Using the Radar Echo Area Time Integral. J. Appl. Meteor., vol. 28, pp. 1162-1175.
- Mintz, Y., 1981. A Brief Review of the Present Status of Global Precipitation Estimates. Precipitation Measurements from Space - Workshop Report. D. Atlas and O.W. Thiele, eds., 1981. NASA/GSFC, pp. D1-D4.
- Mugnai, A., H. J. Cooper, E. A. Smith, and G. J. Tripoli, 1990. Simulation of Microwave Brightness Temperatures of an Evolving Hail Storm at SSM/I Frequencies. Bull. Amer. Meteor. Soc., vol. 71, pp.1-13.
- Olson, W. S., 1987. Estimation of Rainfall Rates in Tropical Cyclones by Passive Microwave Radiometry. Ph.D. Thesis. University of Wisconsin. Madison, WI. pp. 292.
- Petty, G. W., and K. B. Kastaros, 1990. Precipitation Observed Over South China Sea by the Nimbus 7 Scanning Multichannel Microwave Radiometer During Winter MONEX. J. Appl. Meteor., vol. 29, pp. 273-287.
- Prabhakara, C., G. Dalu, R. C. Lo, and N. R. Nath, 1977. Remote Sensing of Seasonal Distribution of Precipitable Water Vapor Over the Oceans and the Inference of Boundary-Layer Structure. Mon. Wea. Rev., vol. 107, pp. 1388-1401.
- Prabhakara, C., G. Dalu, and B. E. Vollmer, 1989. Tropical Oceanic Rainfall: Estimation from SMMR and SSM/I. Preprint Volume - Fourth Conference on Satellite Meteorology and Oceanography, May 16-19, 1989, San Diego, Am. Met. Soc., pp. 79-82.
- Prabhakara, C., D. A. Short, and B. E. Vollmer, 1985. El Niño and Atmospheric Water Vapor From Nimbus 7 SMMR. J. Climate Appl. Meteor., vol. 24, pp. 1311-1324.

- Prabhakara, C., D. A. Short, W. Wiscombe, R. A. Fraser, and B. E. Vollmer, 1986. Rainfall Over Oceans Inferred From Nimbus 7 SMMR: Application to 1982-83 El Niño. J. Climate Appl. Meteor., vol. 25, pp. 1464-1474.
- Prabhakara, C., I. Wang, A. T. C. Chang, and P. Gloersen, 1983. A Statistical Examination of Nimbus 7 SMMR Data and Remote Sensing of Sea Surface Temperature, Liquid Water Content in the Atmosphere and Surface Wind Speed. J. Climate Appl. Meteor., vol. 22, pp. 2023-2037.
- Rao, M. S. V., W. V. Abbot III, and J. Theon, 1976. Satellite Derived Global Oceanic Rainfall Atlas (1973 and 1974). NASA SP-410, Washington DC.
- Reed, R. K., and W. P. Elliott, 1979. New Precipitation Maps for the North Atlantic and North Pacific Oceans. J. Geophys. Res., vol. 84, pp. 7839-7846.
- Savage, R. C., 1976. The Transfer of Thermal Microwaves Through Hydrometeors. Ph.D. Thesis, Univ. of Wisconsin-Madison, pp. 147.
- Simpson, J., 1988. Tropical Rainfall Measurement Mission (TRMM): Report of the Science Steering Group. NASA/GSFC, Greenbelt, MD. pp. 94.
- Smith, E. A., and A. Mugnai, 1988. Radiative Transfer Through a Precipitating Cloud at Multiple Microwave Frequencies. Part II. Results and Analysis. J. Appl. Meteor., vol. 27, pp. 1074-1091.
- Smith, E. A., and A. Mugnai, 1989. Radiative Transfer Through a Precipitating Cloud at Multiple Microwave Frequencies. Part III. Influence of large ice particles. J. Meteor. Soc. Japan, vol. 67, pp. 739-755.
- Spencer, R. W., H. M. Goodman, and R. E. Hood, 1989. Precipitation Retrieval Over Land and Ocean With the SSM/I, Part I: Identification and Characteristics of the Scattering Signal. J. Atmos. Oceanic Tech., vol. 6, pp. 254-273.

- Tsang, L., J. A. Kong, E. Njoku, D. H. Staelin, and J. W. Waters, 1977. Theory for Microwave Thermal Emission From a Layer of Cloud or Rain. IEEE Trans. on Anten. and Prop., vol. AP-25, No. 5, pp. 650-657.
- Tucker, G. G., 1961. Precipitation Over the North Atlantic Ocean. Quart. J. Roy. Met. Soc., vol. 87, pp. 147-158.
- Wilheit, T. T., 1979. A Model for the Microwave Emissivity of the Ocean's Surface as a Function of Wind Speed. IEEE Trans. Geosci. Electron., GE 4, pp. 244-249.
- Wilheit, T. T., A. T. C. Chang, and L. S. Chiu, 1991. Retrieval of Monthly Rainfall Indices from Microwave Radiometric Measurements Using Probability Distribution Functions. J. Atmos. Oceanic Tech., vol. 8, pp. 118-136.
- Wilheit, T. T., A. T. C. Chang, M. S. V. Rao, E. B. Rodgers, and J. S. Theon, 1977. A Satellite Technique for Quantitatively Mapping Rainfall Rates Over Oceans. J. Appl. Meteor., vol 16., pp. 551-560.
- Wu, R., and J. A. Weinman, 1984. Microwave Radiances From Precipitating Clouds Containing Aspherical Ice, Combined Phase, and Liquid Hydrometeors. J. Geophys. Res., vol. 89, pp. 7170-7178.



National Aeronautics and
Space Administration

Report Documentation Page

1. Report No. NASA TM-104546		2. Government Accession No.		3. Recipient's Catalog No.	
4. Title and Subtitle Rainfall Estimation Over Oceans From Scanning Multi-channel Microwave Radiometer and Special Sensor Microwave/Imager				5. Report Date August 1991	
				6. Performing Organization Code 913	
7. Author(s) C. Prabhakara, G. Dalu, G. L. Liberti, J. J. Nucciarone, and R. Suhasini				8. Performing Organization Report No. 91B00126	
				10. Work Unit No.	
9. Performing Organization Name and Address Goddard Space Flight Center Greenbelt, Maryland 20771				11. Contract or Grant No.	
				13. Type of Report and Period Covered Technical Memorandum	
12. Sponsoring Agency Name and Address National Aeronautics and Space Administration Washington, D.C. 20546-0001				14. Sponsoring Agency Code	
15. Supplementary Notes C. Prabhakara : Goddard Space Flight Center, Greenbelt, Maryland G. Dalu and G. L. Liberti: C.N.R. - Istituto di Fisica dell'Atmosfera, Rome, Italy J. Nucciarone: ST Systems Corporation (STX), Lanham, Maryland R. Suhasini: USRA, NASA/GSFC, Greenbelt, Maryland					
16. Abstract The brightness temperature (T_b) measured at 37 GHz shows relatively strong emission from rain, and only marginal effects caused by scattering by ice above the rain clouds. At frequencies below 37 GHz, where the fov is larger and the volume extinction coefficient is weaker, it is found that the observations do not yield appreciable additional information about rain. At 85 GHz ($\text{fov} \approx 15$ km), where the volume extinction coefficient is considerably larger, direct information about rain below the clouds is generally masked. Based on the above considerations, 37 GHz observations with a 30 km fov from SMMR and SSM/I are selected to develop an empirical method for the estimation of rain rate. In this method, the statistics of the observed T_b 's at 37 GHz in a rain storm are related to the rain rate statistics in that storm. The underestimation of rain rate, arising from the inability of the radiometer to respond sensitively to rain rate above a given threshold, is rectified in this technique with the aid of two parameters that depend on the total water vapor content in the atmosphere. The retrieved rain rates compare favorably with radar observations and monthly mean global maps of rain derived from this technique over the oceans are consistent with climatology.					
17. Key Words (Suggested by Author(s)) Microwave Remote Sensing of Rain Rain Statistics Rain Area Polarization				18. Distribution Statement Unclassified Subject Category 47	
19. Security Classif. (of this report) Unclassified		20. Security Classif. (of this page) Unclassified		21. No. of pages 70	
				22. Price	

